SITE CHARACTERIZATION REPORT
SBIK: Biel/Bienne (BE), Kongresshaus/Palais des Congrès

Paolo Bergamo, Manuel Hobiger, Donat Fäh
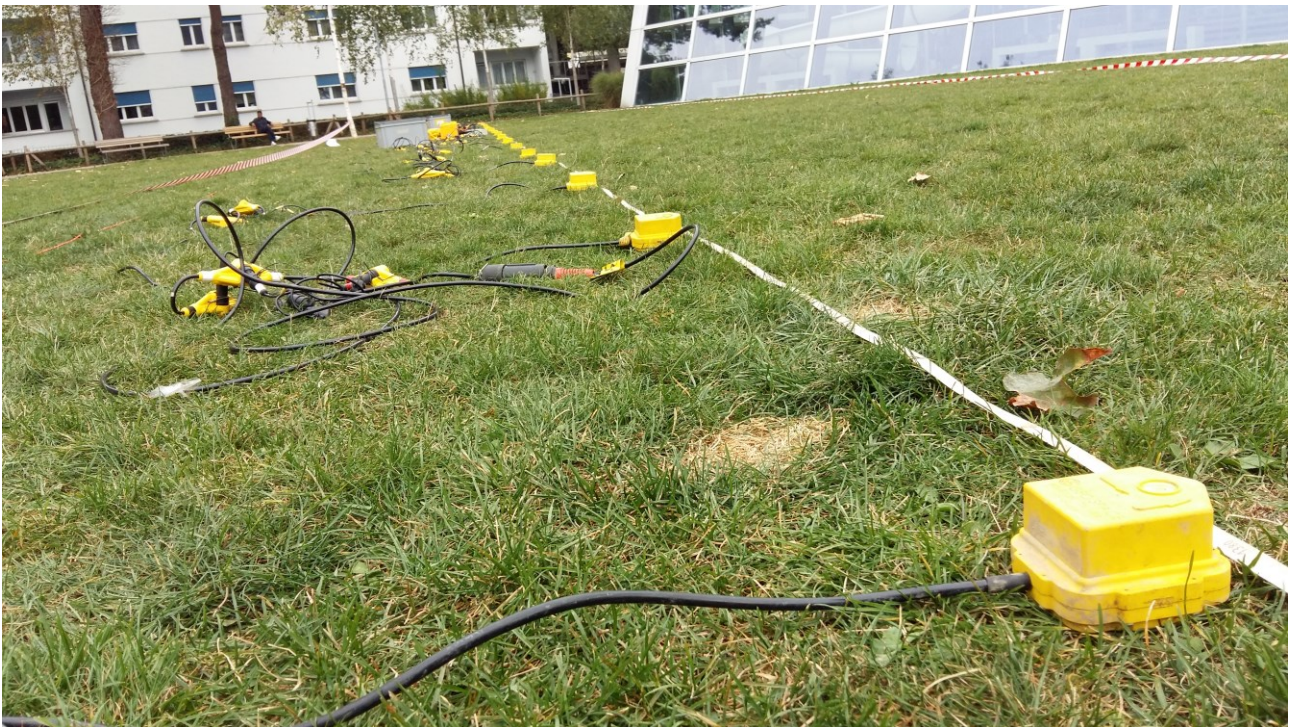
Last modification: 14.05.2018

Contents

Summary

The new SSMNet station SBIK has been installed (11.11.2014) close to the Kongresshaus/Palais des Congrès of the municipality of Biel/Bienne, in the city centre. Active seismic measurements, as well as a single-station noise recording survey, were performed to characterize the subsurface structure beneath the station. The site is characterized by a low fundamental frequency (0.7 Hz) which can be related to the interface between the Swiss molasse and the underlying upper part of the Malm group (marls of Jurassic period). According to available geological information, the boundary should be located at a depth of approximately 700 m; the inversion of the acquired seismic data is in agreement, indicating a depth of 620-800 m. Another peak of the amplification function is located at 1.2 Hz, which is due to the impedance contrast between the thick cover of aggradation sediments (estimated to extend down to 155-180 m depth), and the Molasse formation below. Nonetheless, the dominant feature of the amplification function (and H/V curve) is represented by a peak at 5 Hz, reaching values of amplifications larger than 10; it is to be ascribed to two sharp velocity contrasts, at ~3.8 m between soft turf and gravels below, and at ~8.5 m between the latter and the more compact Juraschotter. The estimated V_{S30} value for the shallower subsurface is 374 m/s, which classifies the soil as B type according to Eurocode 8 (CEN, 2004), and as C type following SIA261 (SIA, 2014).

1.   Introduction.

In the framework of the second phase of the SSMNet (Swiss Strong Motion Network) renewal project, a new station, labelled as SBIK, was installed on 11.11.2014 in vicinity of the Kongresshaus of the municipality of Biel (Figure 1a). The city rests on a basin of quaternary aggradation sediments, bottomed by the Swiss Molasse. The location of SBIK in the city centre of Biel (hence in an area with considerable artificial noise sources and very high building density), makes it relatively unsuitable for the execution of passive array recordings. Therefore, active seismic surveys and a single-station H/V measurement were carried out to ensure the seismic characterization of the site.

2.   Geological setting

The site is located on the top of a basin of quaternary (Holocene) aggradation sediments, according to the geological information from the Swiss Office of Topography (1:25000 Swiss Geological Atlas, Figure 1b). Gravimetric measurements, available only for the south-east area of Biel (again from Swisstopo, Klingelé 2012, Figure 2), indicate that the interface with the Molasse below is characterized by a steep gradient, degrading from north-east (bedrock depth 0-20 m) to south-west (bedrock depth 161-240 m).

This feature seems to be confirmed by the appearance of the H/V curves retrieved in a campaign of single-stations noise recordings conducted by SED in 2013 for the area of Biel. The insets to the left, right and bottom of Figure 2 display some sample H/V curves; the peaks related to the sediments/Molasse boundary decrease from approximately 1.3 Hz in the north-east (close to SBIK) to ~1.0 Hz in the south-west (stations near Lake Biel; here this peak becomes hardly distinguishable from the 0.7 Hz peak associated to the Molasse-Malm group interface). Station SBIK is located at the border between the areas where the bedrock is expected in a range of 20-80 m and 81-160 m (central panel in Figure 2). Interestingly, the H/V curves (from various methods) obtained from the single station measurement performed for the characterization of station SBIK present a peak at 1.2 Hz (see top panel in Figure 2), consistently with its correlation with the degrading sediments/Molasse interface proposed above; the interpretation of H/V measurement is anyhow discussed with greater detail later in the report (section 4).
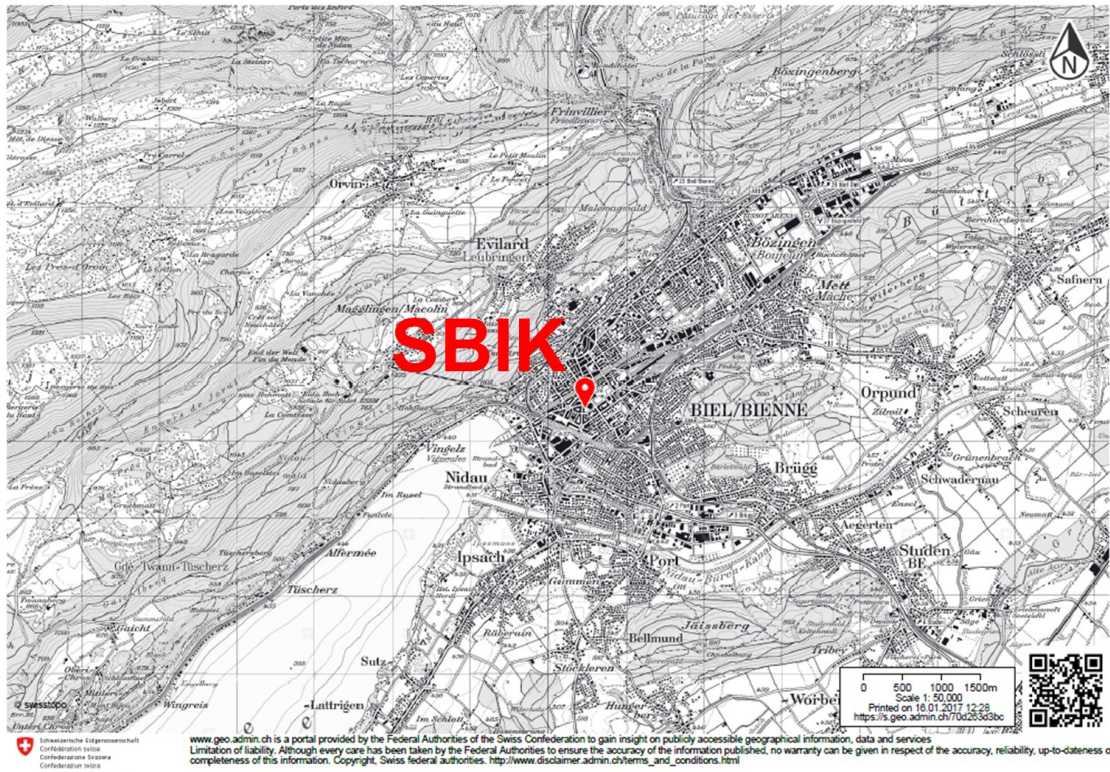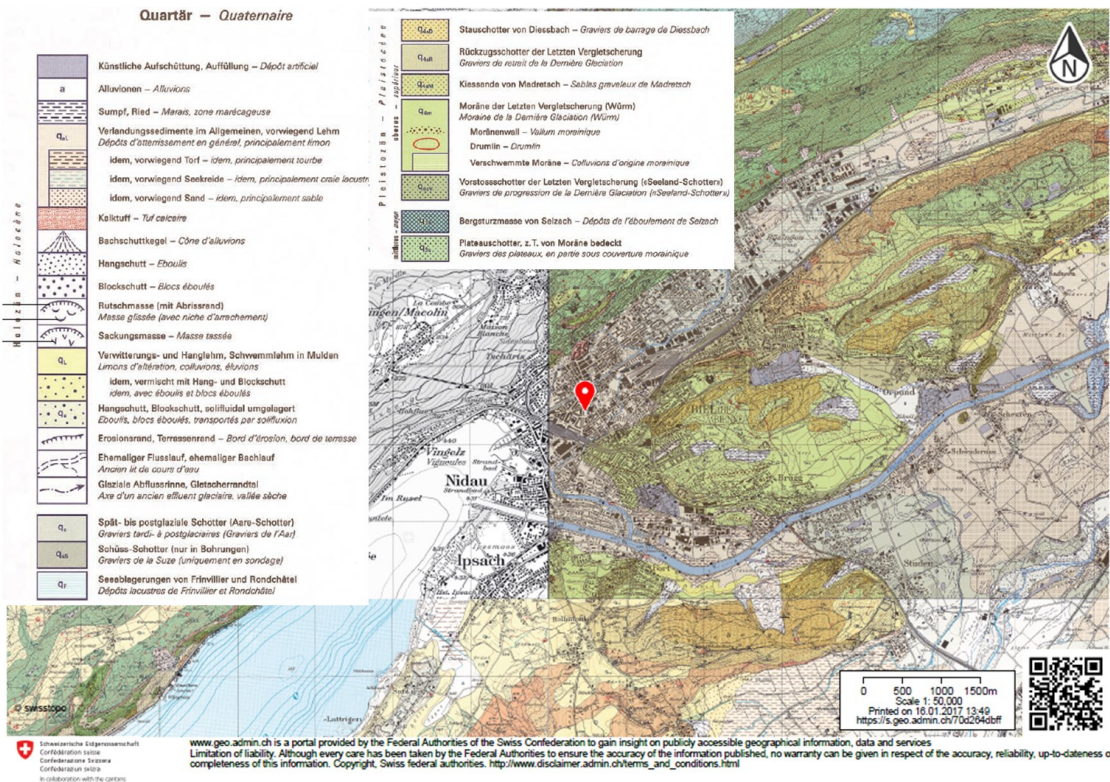
Figure 1 – a) position of SBIK in the urban area of Biel, and b) on the 1:25000 Swisstopo Geological Atlas map. (© 2017 Swisstopo, JD100042).
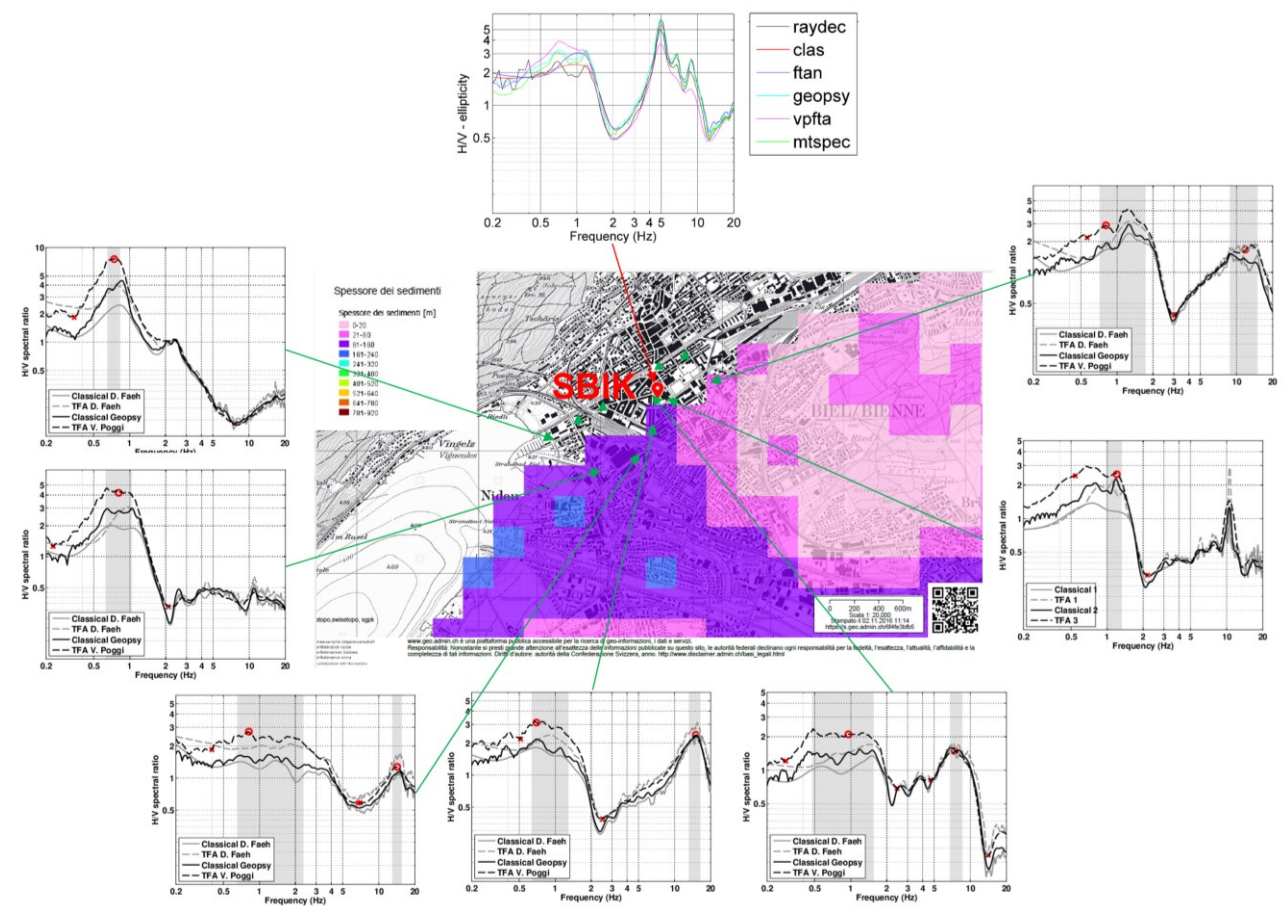
Figure 2 – Central panel: map of the depth of the bedrock interface as estimated by gravimetric measurements (© 2017 Swisstopo, JD100042). Left, right and bottom insets: H/V curves obtained from single-station passive seismic measurements conducted by SED in 2013 (location of the corresponding station indicated by a green arrow). Top: H/V curves from the single-station measurement carried out for the site characterization of SBIK (in close proximity to station SBIK).

3. Active seismic measurements

Station SBIK is located on the western side of a public green area in the city centre of Biel. The active seismic array was deployed along the diagonal of this area (therefore stretching in north–south direction, Figure 3), to maximize its length and therefore its wavelength coverage.

For the sake of a comprehensive subsurface characterization, multichannel analysis of surface waves (MASW; Park et al., 1999) and P-/SH-wave refraction (Redpath, 1973) surveys were conducted.

3.1 Equipment

We used three sets of eight three-component geophones (4.5 Hz corner frequency). Each geophone set was connected to a Geode datalogger; the three Geodes were coupled for time synchronization. The seismic source was 5-kg sledgehammer, hitting at four source locations (src1-4; red stars in Figure 3) two types of metal plates:

i)   a flat square plate, for P-SV wave excitation: the hammer was released vertically on the plate;

ii)   a wedge-shaped metallic frame, for SH wave excitation. The plate is an isosceles right triangle: the hypotenuse is placed on the ground, and coupled to it with spikes penetrating the soil. The catheti are oriented orthogonally to the geophone spread, and alternately hit with the hammer (see top of Figure 5).

As for the last source point (src5), only the flat plate was employed.

The synchronization between the traces recorded by the geophones and the seismic source was ensured by a trigger device fastened to the hammer handle.

Figure 3 – Map representing the position of the targeted station (SBIK), of the active seismic line and of the noise recording sensor (labelled H/V; © 2016 GoogleMaps).

3.2 Geometry of the acquisition array

The seismic line was constituted by 24 3-component receivers, aligned at regular intervals of 1.7 m, for a total length of 39.1 m. The geophones were laid on the soil of the green area, with metal spikes ensuring a firm coupling with the ground (Figure 4).

As earlier anticipated, MASW and P-/SH- wave refraction measurements were performed. As for refraction surveys, the sources were placed at four locations along the receivers' line: at the south end, at one and two thirds of the spread, and at the north end (src1-4, Figure 3). The seismic sections acquired with the source at two extremities of the array were exploited for surface (Love) wave

analyses, as well, after the removal of the near-offset traces (source-receiver distance < 5.1 m; Socco and Strobbia, 2004). An additional MASW-only shooting position was placed south of the array, 11.9 m from the closest geophone (Figure 3, src5). In this case, the whole dataset from 24 geophones could be exploited for surface wave analysis (the maximum recordable wavelength was assumed to be 78.2 m, i.e. twice the array length; Socco and Strobbia, 2004). Due to logistical constraints, it was not possible to deploy the source in a symmetrical position north of the array (off-end shooting, typical configuration for MASW acquisition: see for instance Ivanov et al., 2004).

Figure 4 – Geophone array in place.

3.3   Acquisition

The time-sampling parameters adopted for both MASW and refraction acquisitions were the following: sampling interval = 62.5 µs, record length = 1 s, pre-trigger delay = -0.1 s. At the source points src1-4, 30 hammer blows were successively shot: 10 hitting the flat plate, 20 hitting the wedge-shaped plate (10 blows on each side). As earlier anticipated, in src5 only 10 vertical hits were struck. For each hammer blow, the recordings from all geophones were saved in a separate *.sg2* file. In Figure 5, seismic sections acquired for the source at the south end of the geophones array (src1) are represented. The panels in the left column correspond to hammer blows on the flat plate; the center and right column refer to the hammer impacts on the two sides (facing east and west) of the triangular plate. As shown by the seismic sections in Figure 5, few recording channels are malfunctioning; the corresponding traces were discarded or muted in the successive processing steps.
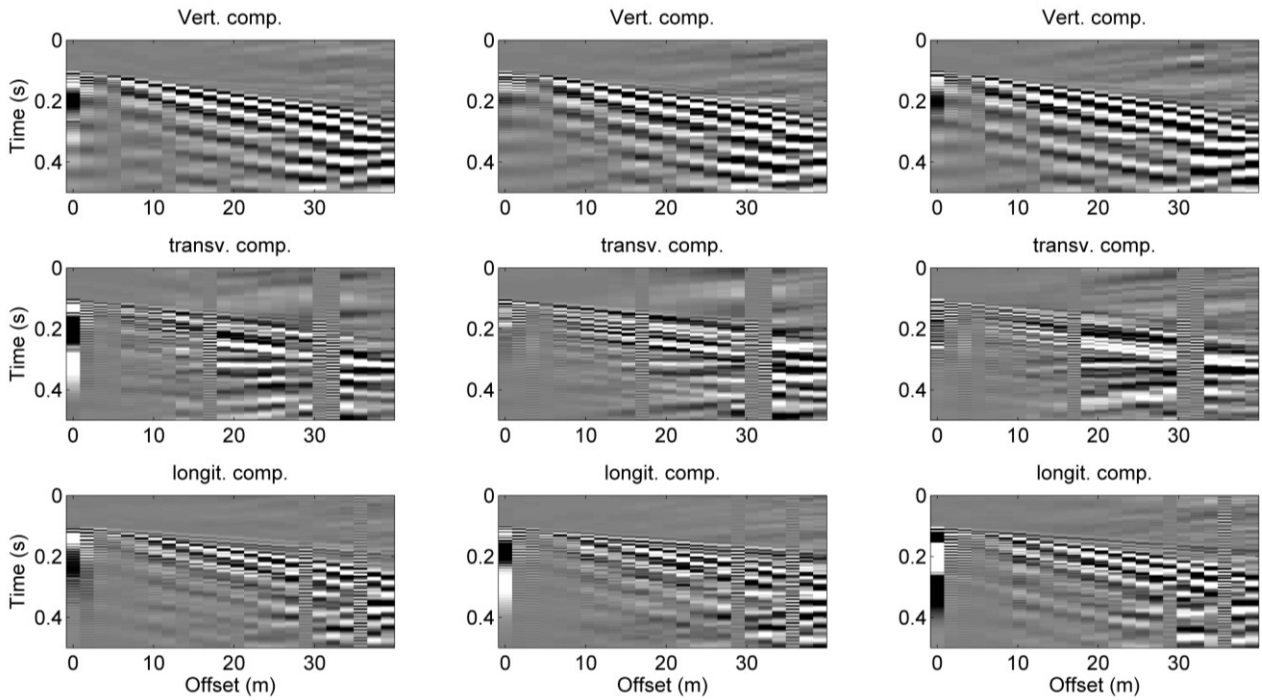
Figure 5 – Seismic sections acquired with the source at the south end of the geophones array (src1 position). The panels in the left column correspond to hammer blows on the flat plate; the center and right column refer to the hammer strokes on the two sides (facing approx. east and west) of the triangular plate.

3.4 Processing

3.4.1 Pre-processing

Seismic traces generated by different shots, with the same seismic source at the same location (10 sets for each configuration), were summed - or stacked - in time domain. This was done to enhance the coherent seismic events generated by the controlled seismic source, and at the same time to minimize the incoherent noise anyhow present in the recordings (Foti et al., 2015). "Stacked" seismic sections, with greater signal-to-noise ratio, were hence obtained (Figure 6). To preserve the effectiveness of the stacking operation, the vertical components of the seismic traces at short offsets were cross-correlated to ensure a robust synchronization among the seismograms to be later superimposed.
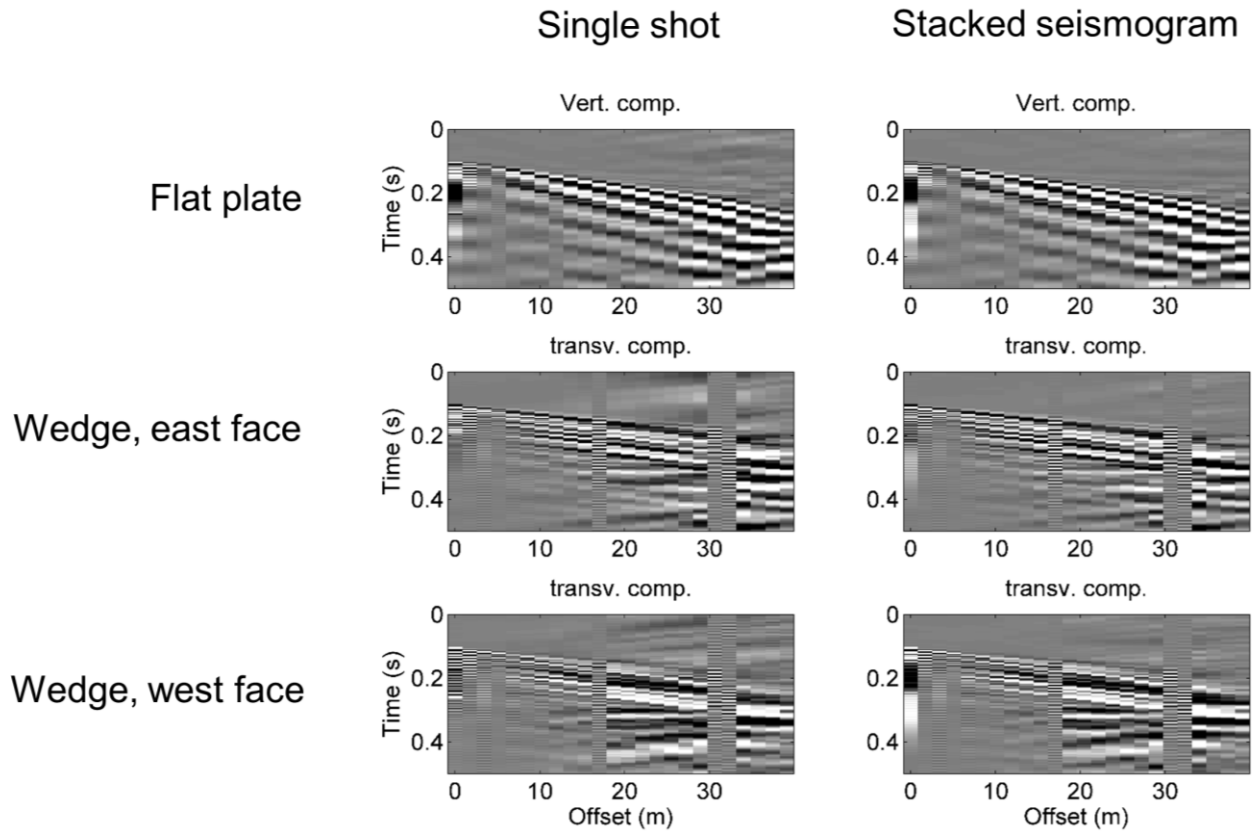
Figure 6 – Single-shot (left column) and stacked seismograms (right column) obtained with different source types and for different geophone components.

The hammer blows exerted on the slant faces of the wedge apply a two-component excitation to the ground: a vertical and a horizontal component, the direction of the latter depending on which face of the plate the stroke is given. Therefore, by summing the seismic traces obtained hitting the wedge on the two sides, the effects of the horizontal components are mutually eliminated, while the vertical components interact constructively; by computing the difference of the corresponding seismograms, the vertical components nullify each other, while the horizontal components interact constructively (Schmelzbach et al., 2016; Sollberger et al., 2016). Consequently, the sum operator is equivalent to the use of a vertical blow; the difference operator is equivalent to a pure shear source. This is shown in Figure 7, where the vertical component seismogram, obtained using a vertical hammer blow hitting the flat plate (left panel), is compared to the seismic section derived by summing the traces recorded when successively hitting the two faces of the wedge (centre panel). The marked similarity between the two seismograms confirms the validity of the process. The panel to the right in Figure 7 represents the section obtained by computing the difference of the transversal component traces acquired when using the wedge-shaped plate (hence this common shot gather corresponds to a solely SH excitation). This seismogram and the others similarly obtained by moving the source to other shooting positions were later exploited for SH-wave refraction and Love wave analyses.
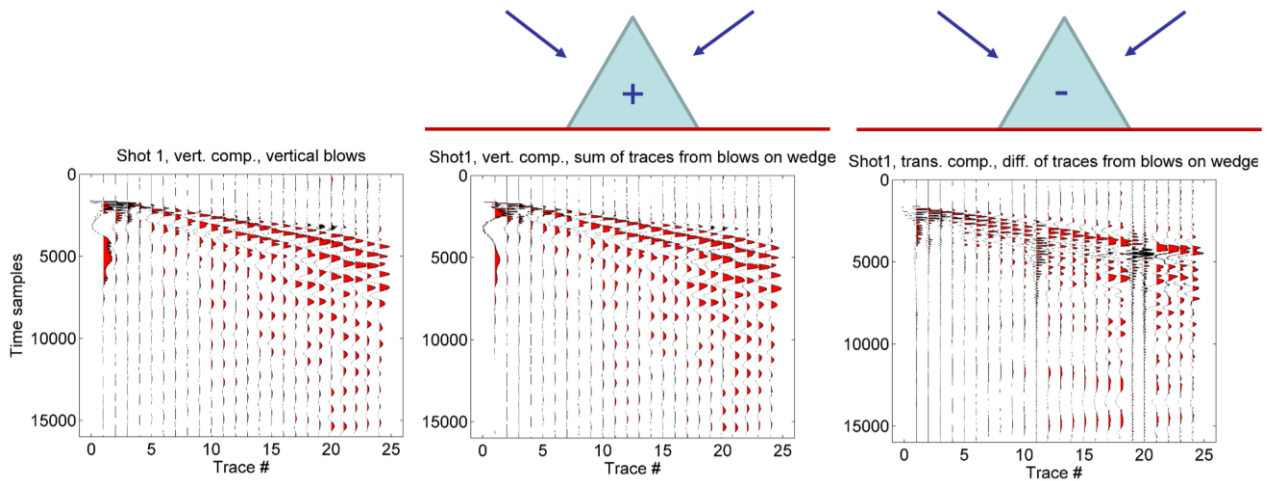
Figure 7 – Left panel: vertical component common shot gather obtained when applying a vertical hammer blow on the flat plate. Centre panel: sum of vertical component traces recorded when hitting the hammer on the two faces of the wedge. Right panel: difference of transversal component traces recorded when hitting the hammer on the two faces of the wedge.

3.4.2 Refraction processing and interpretation

P-wave first-break arrival times were manually picked on the stacked seismograms representing the vertical component of soil surface vibration. Figure 8a represents a sample seismic section and the identified first-breaks; the complete set of obtained travel-time curves (one for each considered shooting position) is shown in Figure 8b. The hodocrones appear to be approximately symmetrical, i.e. the P-wave travel time depends only on the source-to-receiver distance and not on the position of the shot point. This suggests a 1D geometry (no lateral variations) for the near-surface below the active seismic arrays.

As for SH-wave arrivals, these were picked on the seismic sections obtained by computing the difference between the transversal component seismograms recorded when hitting the wedge-shaped plate on the two opposite faces (see previous section; Figure 8c shows a picking example). The complete set of four SH-wave hodocrones (one from each considered shooting position) is displayed in Figure 8d.
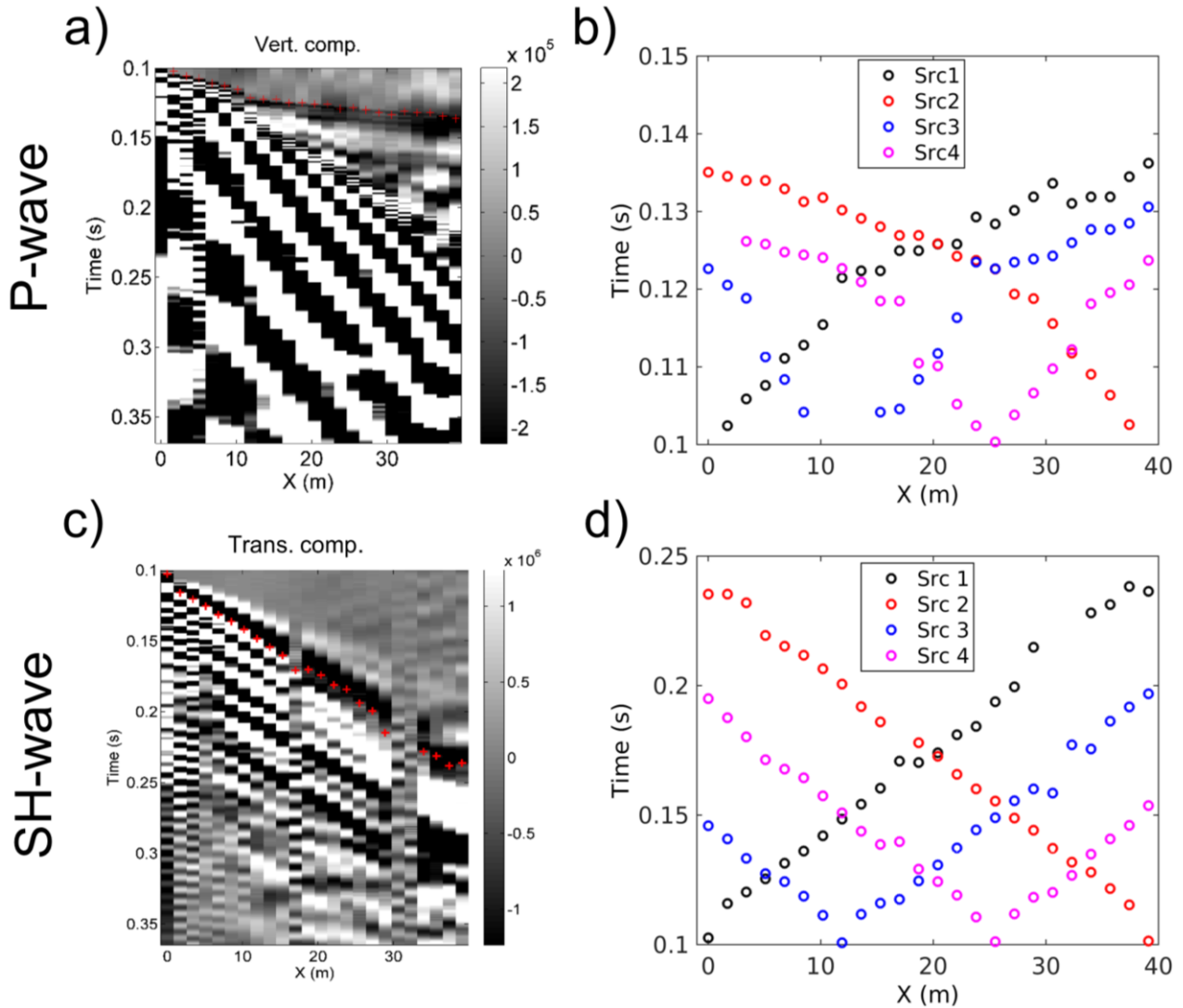
Figure 8 – P- and SH-refraction processing. a) Example of picking of first break P-wave arrivals; b) obtained P-wave travel time curves. c) Example of picking of first break SH-wave arrivals; d) obtained SH-wave travel time curves. The X coordinate in Figure (b) and (d) runs along the geophone spread, from its south (X = 0 m) to its north end (X = 39.1 m).

Collected refraction data were interpreted with the method of intercept time analysis (Reynolds, 2011). Following the hypothesis of a 1D geometry for the shallow subsurface (see above), the hodocrones obtained from refraction processing (Figures 8b, 8d) were collapsed into two travel-time curves (one for P-waves, one for SH-waves) in time-offset domain (circles in Figures 9a,9b).

As for P-wave travel times (Figure 9a), these clearly follow a bi-linear trend, with direct arrivals (offset < 12 m) showing a velocity for the surficial layer of 525 m/s; refracted arrivals (at offset > 12 m) travel at a speed of 1932 m/s, which suggests the presence of a deeper saturated layer. The possible presence of a velocity inversion (i.e. a softer layer embedded between stiffer formations), as indicated by the appearance of the Rayleigh wave dispersion curves and available geological data (see following sections), contradicts the assumption of intercept time analysis (Whiteley and Greenhalgh, 1979); hence, it was not possible to determine here the thickness of the surficial layer, as well as the expected depth of the water table.

SH-wave travel times (Figure 9b), beyond a very short offset threshold for direct arrivals (X < 2 m, V_S of surficial layer = 133 m/s), align along a linear trend suggesting a deeper layer with V_S of 296 m/s. In this case, considering the very short cross-over distance (2 m), corresponding to a thin thickness for the shallowest layer of 0.5 m, this simple two-layer S-wave velocity model can be assumed to represent the V_S of the subsurface above the velocity inversion (therefore the estimation of the interface depth between surficial layer and halfspace can be retained).
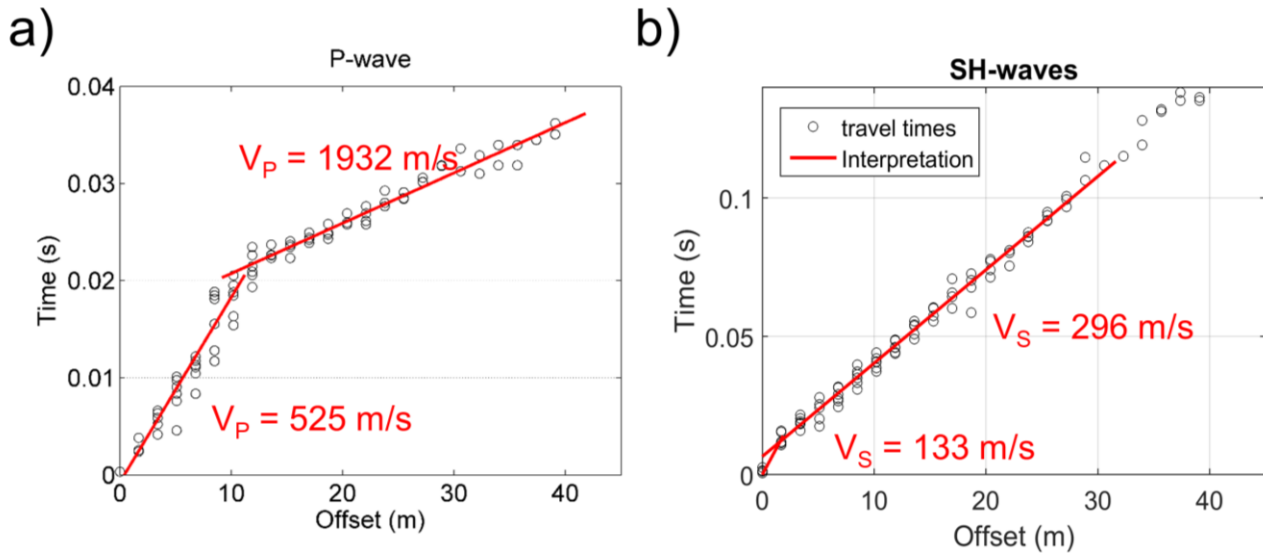

Figure 9 – P- and SH-wave travel time interpretation

3.4.3   Rayleigh wave data f-k processing

Rayleigh wave dispersion data were extracted from the vertical and longitudinal component seismograms for MASW acquisitions, recorded when using the sledgehammer vertically striking the flat plate, positioned at src5 (Figure 3). As anticipated in section 3.2, this shooting position has in fact a sufficient offset from the closest receiver (11.9 m), so that the whole array of receivers can be considered for *f-k* MASW processing (minor influence of near-field effects: Foti et al., 2015). The considered seismic sections were processed by means of a 2D *f-k* (frequency – wavenumber) transform (Socco and Strobbia, 2004), in order to obtain a conversion of the recorded sets of traces from time–offset to frequency–wavenumber domain. *f-k* panels from single shot records with the same source position were summed to obtain spectral images with greater S/N ratio (O'Neill, 2003; Neducza, 2007). The energy maxima corresponding to the Rayleigh wave dispersion curves were picked on these stacked panels; spectral amplitude peaks from individual shot recordings were identified as well, and used to define the uncertainty intervals in the estimation of phase velocities (Socco et al., 2009; Boiero and Socco, 2010).

Figure 10 shows the stacked *f-k* panels from the considered seismic records, as well as the corresponding picked energy maxima. The dominant feature in all *f-k* spectra is an event extending continuously in the 10-90 Hz frequency band, whose corresponding phase velocities increase with frequency (black triangles in Figure 11), from 150 m/s at 10 Hz to 210 m/s at 90 Hz. This feature is generally associated to a velocity inversion (softer layer embedded within a stiffer formation) in the shallow subsurface, which for SBIK site could correspond to the presence of a surficial turf layer, as

indicated by local geological information from borehole logs (see section 6). Many authors have observed that this feature is not a proper Rayleigh wave mode, but an apparent dispersion curve produced by the fact that, in presence of velocity inversion, surface wave energy tends to "leak" from lower to higher order modes as the frequency increases (Tokimatsu 1997; Foti et al., 2000; Socco and Strobbia, 2004; Maraschini and Foti 2010). Therefore, only the data points belonging to this slowest branch and around the "kink" where phase velocities first decrease with frequency and then sharply increase, could be attributed to the fundamental mode of Rayleigh waves (dashed gray line in Figure 11, left panel; see similar examples e.g. in Socco and Strobbia, 2004, Maraschini and Foti, 2010, Foti et al., 2015). Beside this limited segment, it is not possible to univocally attribute other data points from the extracted apparent curve to a definite Rayleigh wave propagation mode; the operation of mode-numbering is therefore postponed to a later phase (section 3.4.6).
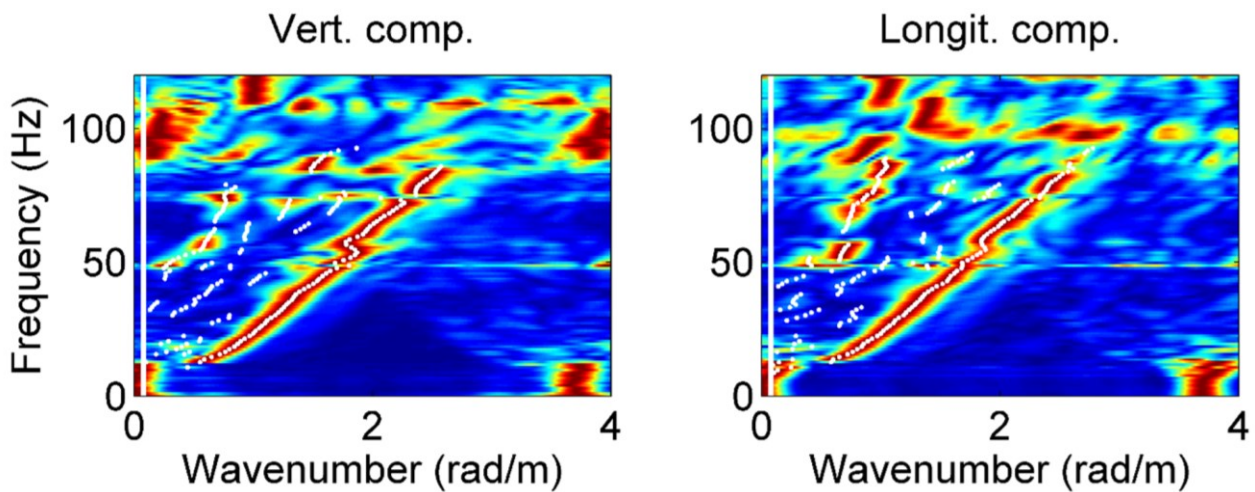

Figure 10 – Stacked normalized f-k spectra obtained from vertical and longitudinal components of the seismic section with source positioned in src 5. The white vertical line on the left side of the panels indicate the resolution limits (minimum wavenumber). White dots are the picked energy maxima, corresponding to Rayleigh wave dispersion curve data points.

3.4.4   WaveDecActive

Seismic traces acquired when using the sledgehammer vertically hitting the flat plate in src1 or 2 were also processed with the WaveDecActive code (Maranò et al., 2017), with the aim of retrieving the properties of Rayleigh wave propagation in terms of both phase velocity and ellipticity. WaveDecActive implements a maximum likelihood algorithm for the analysis of Rayleigh waves generated by a controlled source. Differently from the more conventional *f-k* analysis approach (3.4.3), it is able to characterize the Rayleigh wave propagation both in terms of phase velocity and ellipticity angle. Key parameters required by WaveDecActive are the definition of the maximum number of Rayleigh waves that the code attempts to identify, and the value of parameter γ, which is able to modify the approach of the code towards wave identification from a Bayesian information criterion ($\gamma=1$) to a maximum likelihood approach (ML, $\gamma=0$), or a compromise between the two ($0<\gamma<1$). Following the recommendations of the code's author (Maranò, 2016) and some preliminary attempts, the maximum number of waves was set to 3, and γ to 0.1, thus opting for an approach close to a maximum likelihood solution.

14

The obtained results are displayed in Figure 11, showing the estimated Rayleigh wave phase velocities (blue and red dots in the left panel) and ellipticities (right panel) for the considered shots.
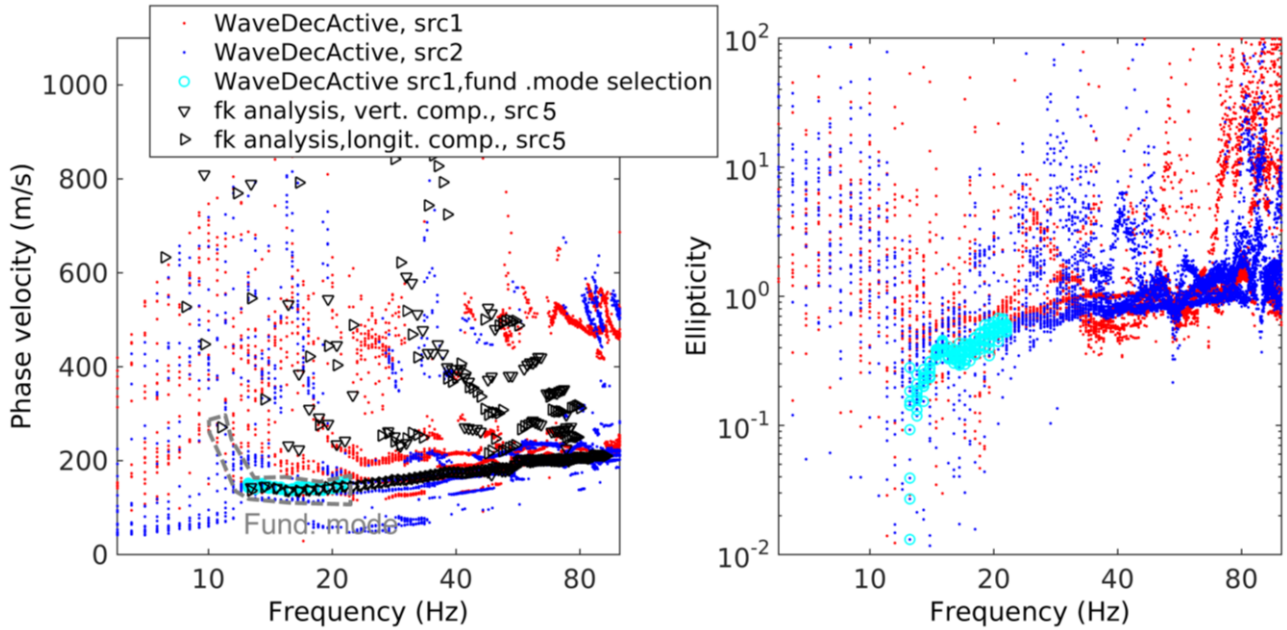

Figure 11 – Extraction of Rayleigh wave dispersion and ellipticity curve. Left: estimated values of phase velocities. Black triangles refer to data points obtained from the f-k analysis of src5 seismic sections (vertical and longitudinal component; see also Figure 10). The branch attributed to the fundamental mode is highlighted with a dashed gray line. Red and blue dots represent the phase velocity values obtained with WaveDecActive: highlighted with cyan circles are the points attributed to the Rayleigh wave fundamental mode. Right: estimated values of Rayleigh wave ellipticity, obtained from WaveDec-Active. The color code is the same as in the left panel.

As observed in the *fk* analysis results (3.4.3), the dominant feature in the phase velocity-frequency plane (Figure 11, left panel) is a bundle of branches, probably apparent modes, with increasing phase velocities with frequency, from approximately 120 m/s at 15 Hz to 220 m/s at 100 Hz. At higher phase velocities (300 – 700 m/s), several branches with steep negative slope were identified. Hence, the overall trend is the same retrieved with *fk* analysis, although the agreement on individual phase velocity data points is poor. This can be explained, at least partially, with the peculiar behavior of Rayleigh wave propagation in case of shallow velocity inversions; as described in 3.4.3, in these cases the energy "leaks" from lower to higher order modes as frequency increases, therefore identifying and following individual modes is cumbersome when applying either *fk* analysis or a ML approach (WaveDecActive). Nevertheless, in the frequency range 12 – 20 Hz a good agreement was observed between WaveDecActive (src1 data) phase velocities and the segment identified as fundamental from *fk* analysis (see Figure 11, left panel, cyan circles). Confirming their identification as fundamental mode, these data points have negative values of ellipticity angle (i.e. retrograde particle motion; Maranò et al., 2017).

3.4.5 Love wave data f-k processing

As for the extraction of Love wave dispersion data, 2D *f-k* analysis was applied to the seismograms obtained as the sum (i.e. stack) of the differences between the transversal component traces acquired when alternately hitting the two opposite faces of the wedge-shaped plate (these seismic sections should portray, as explained in 3.4.1, a pure SH excitation). In this case the stacking operation was performed, similarly to SH-refraction and differently from Rayleigh wave processing, in time-offset domain. In fact, to reproduce the effect of an SH source, the difference operation presupposes similar spectral energy content between the seismic recordings that are subtracted; this assumption is indeed more robust when considering altogether (through a stacking operation) the single-shot seismograms. Figure 12a shows the *f-k* panels obtained from the two shooting positions suitable for MASW (Love) analyses (src1 and src2, Figure 3), as well as the picked energy maxima. Similarly to Rayleigh wave, also in the case of Love waves the energy "jumps" towards higher modes as the frequency increases, and none of the identified modes extends across a wide frequency band (Figure 12b). Data points belonging to the slowest dispersive branch were reasonably attributed to the fundamental mode of Love wave propagation (dashed contour line in Figure 12b); for the other branches, no mode numbering was attempted.
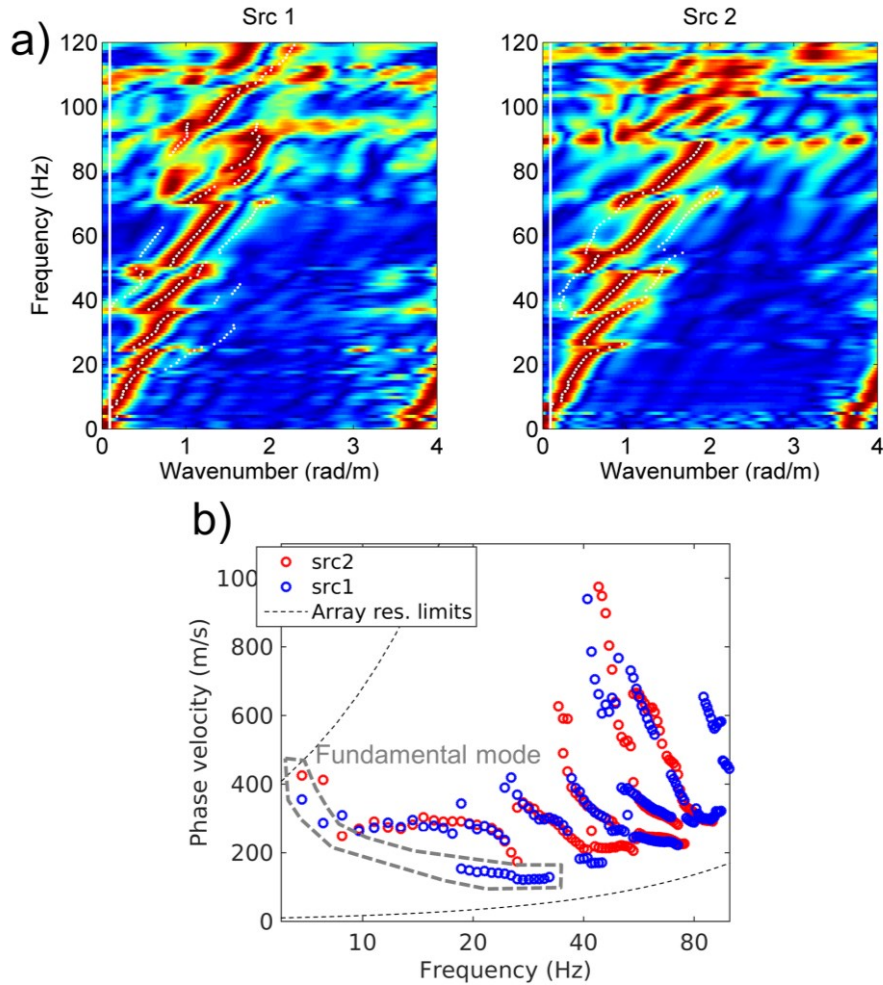
Figure 12 – Love wave dispersion curve extraction. a) Normalized f-k spectra of the transversal component seismogram, suitable for Love wave dispersion curve identification. Vertical white line: minimum wavenumber. White dots: picked energy maxima; b) picked dispersion curves: data points belonging to the slowest dispersive branch were identified as fundamental mode (dashed contour line).

3.4.6   Mode numbering for Rayleigh wave dispersion curve

As shown in section 3.4.3, the identification of the mode number for the extracted Rayleigh wave dispersion curve is possible only for few data points, in the narrow frequency band 10-20 Hz (Figure 11). For the tentative attribution of the other branches, we implemented and followed an approach inspired by the procedures proposed by Maraschini and Foti (2010) and Abdel Moati et al. (2013), the latter developed to face a case similar to that of SBIK site, i.e. the characterization of sites with a near-surface S-wave velocity inversion with Rayleigh wave data.

The basic idea is to test the agreement between the experimental apparent dispersion curve and a set of synthetic curves corresponding to a vast population of possible subsurface models, assuming a priori only the reliable modal attribution of few data points, and letting the others free to be assigned to the closest (in terms of phase velocity) simulated mode. The synthetic curve that best "explains" (i.e. closely matches) all (or most of) the experimental data points, and therefore achieves the lowest misfit, is assumed to propose the most likely modal attribution.

Therefore, we tested a set of 1500000 multimodal synthetic curves, with modes from fundamental to 5th higher, corresponding to as many randomly generated velocity models. The subsurface was parameterized as a stack of 6 layers + halfspace; wide boundaries were allowed for the random selection of V_S, V_P and thickness values. In fact, the purpose of this process is not inverting for a subsurface model, but rather identify the modal attribution that best explains the experimental data of uncertain mode numbering.

The collation between experimental and synthetic dispersion curves is summarized through the computation of a misfit function, which has the form of a root mean square error (RMSe):

$$RMSe_j = \sqrt{\sum_{i=1}^{n} \left(\frac{d_i - s_{ij}}{w_i}\right)^2} \tag{1}$$

where j refers to the jth multimodal synthetic curve, d_i is the ith data point (out of n) of the experimental dispersion curve, s_{ij} is its counterpart from the jth synthetic curve, and w is the vector of weights for the experimental data. For the phase velocities d_i of certain modal attribution (e.g. those recognized as fundamental mode in 3.4.3, Figure 11), the counterpart s_i is the phase velocity value from the synthetic mode with the same frequency. For the unassigned phase velocities d_i, the counterpart s_i is the closest (in terms of phase velocity) data point having the same frequency: d_i is therefore attributed to the mode having the closest phase velocity at the same frequency. If the relative distance between the unassigned experimental data point and the closest synthetic value exceeds a given threshold (in this case set to 10%), the experimental point is identified as outlier and discarded from the RMSe computation.

It should be noted that, differently from the affirmed approach of Maraschini and Foti (2010), the collation between experimental and simulated data is carried out resorting to the full computation of synthetic curves, which has indeed higher computational costs than the evaluation of the determinant of the Haskell-Thomson transfer matrix (as in Maraschini and Foti, 2010). This heavier cost is anyhow traded for the possibility to constrain a priori some experimental data points to a definite mode, thus better stabilizing the mode numbering process.

In order to further constrain and stabilize the search for the optimal modal attribution, the experimental fundamental mode of Love waves (3.4.5, Figure 12) and the ellipticity of the fundamental mode of Rayleigh waves (3.4.4, Figure 11, left panel) were included in the vector of experimental data d for RMSe computation, both with constrained mode numbering.

Figure 13 shows the 15 best performing sets of synthetic curves (out of a population of 1500000), achieving the minimum misfit. Focusing on Figure 13a (Rayleigh wave dispersion curves, i.e. the target of this process), many of the unattributed data points appear to align along definite synthetic modes; the latter show in general a consistent behavior. As expected in case of shallow V_S velocity inversion (see 3.4.3), the experimental branch with low velocity spanning the whole 10-90 Hz band "jumps" towards higher modes of propagation as frequency increases.

For completeness, we display in Figure 14 the S- and P-wave velocity models corresponding to the 15 best fitting sets of curves from Figure 13. We remark that these profiles do not represent the goal of the described procedure (which is identifying the optimal Rayleigh wave mode numbering instead) and do not represent the inversion result for SBIK site (which is illustrated in the next sections). Nevertheless, the models show some consistency, particularly at shallow depths (< 10 m), where they identify a sharp velocity inversion between 1-4 m depth. This feature is consistent with the presence of a surficial, soft layer of turf in the same depth range, as indicated by local borehole log profiles

(e.g. Figure 22). We also note the consistency between the very shallow portion of the profiles in Figure 14 and the results of the seismic refraction interpretation (we refer to the V_S and V_P of the shallowest layer, and the V_P of the layer below the velocity inversion).
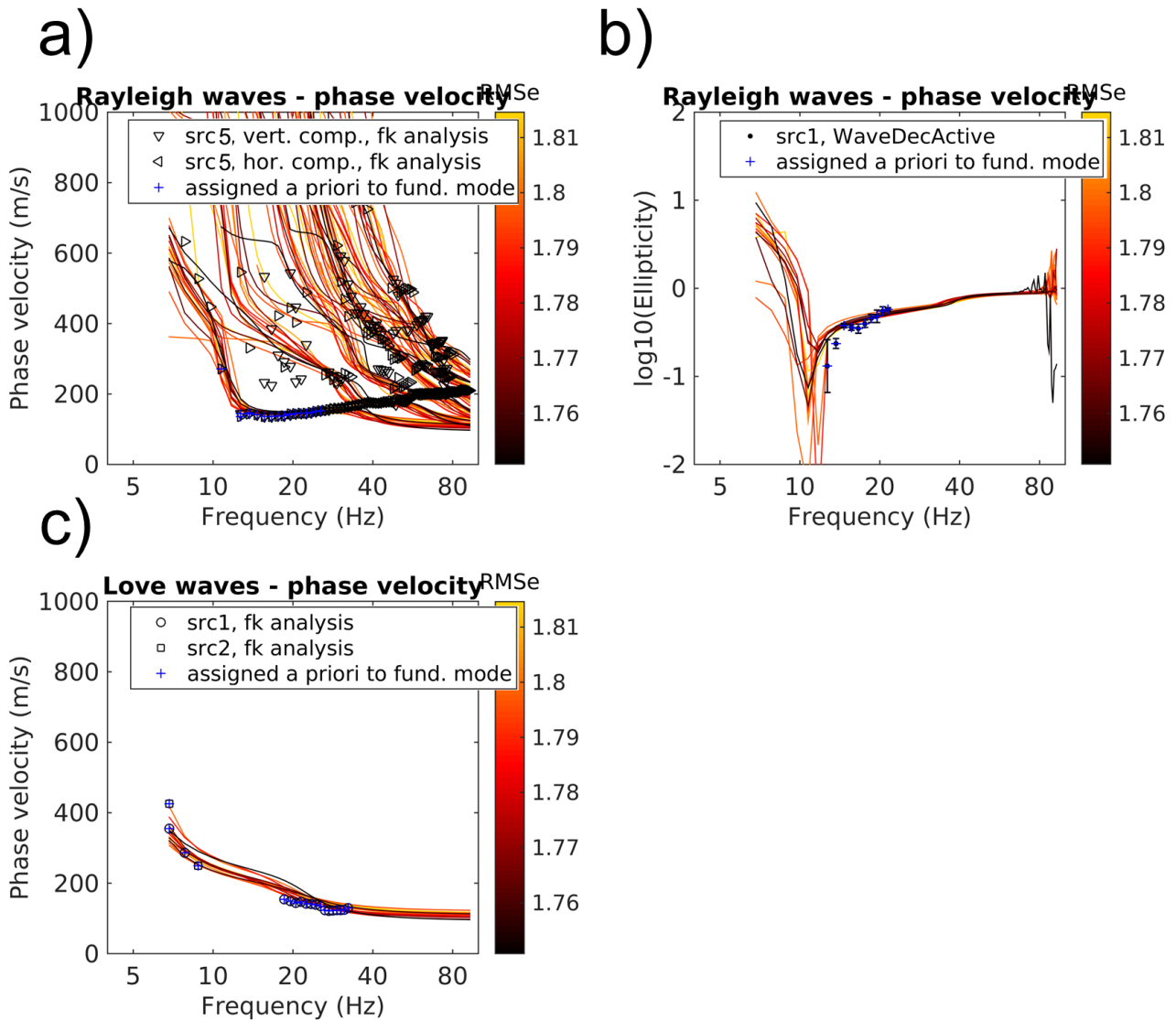

Figure 13 – Fit between experimental curves (black symbols) and the 15 best fitting sets of synthetic curves (color scale). Experimental data points assigned a priori to the fundamental mode of Rayleigh (a, b) and Love (c) waves are indicated with a blue cross. a) Rayleigh wave multimodal phase velocity dispersion curves; b) Rayleigh wave fundamental mode ellipticity; c) Love wave fundamental mode dispersion curves.
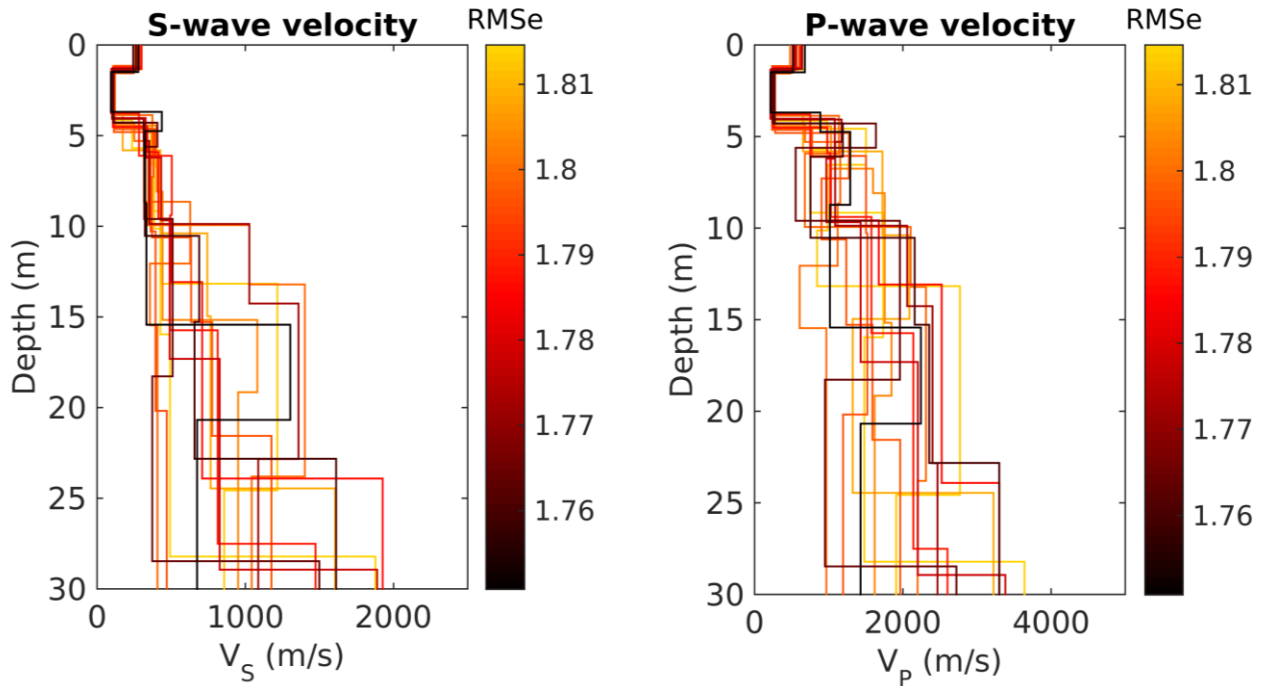
Figure 14 – S- (left) and P-wave (right) velocity models corresponding to the 15 best fitting sets of synthetic curves (Figure 13).

For the modal attribution of the experimental Rayleigh wave dispersion curve, to be assumed for the successive inversion process (next section), we followed this criterion: considering the 15 best performing synthetic multimodal curves (Figure 13a), the ith experimental data point is assigned to a given mode if at least 10 synthetic curves "propose" the same mode numbering, otherwise it is discarded as outlier. The result for the modal attribution are shown in Figure 15.
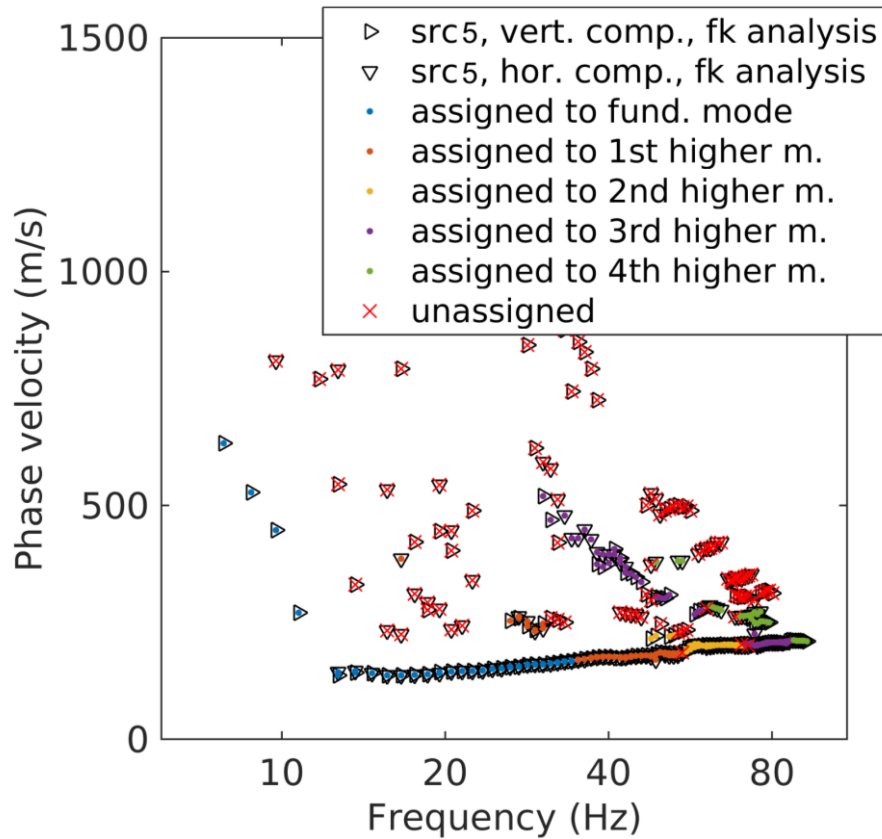
Figure 15 – Assumed mode numbering for the experimental Rayleigh wave dispersion curves obtained from the fk analysis of the seismic sections with source position in src5 (section 3.4.3).

4 Passive seismic measurements

Besides active seismic surveys, a single-station noise recording measurement was performed. A Lennartz 3C 5s seismometer, connected to a Quanterra Q330 datalogger, was deployed in close proximity to station SBIK (Figure 3). The sensor was placed on a metal tripod in a 10 cm deep hole, for a better coupling with the ground. The sampling frequency was 200 Hz, and the recording spanned a 6-hour time interval (in parallel to active surveys). Since the acquisition was performed in an urban environment during daytime (high levels of artificial noise expected), before proceeding to H/V and ellipticity curve computation, we briefly verified whether the recordings have a consistent frequency content over time (as desirable), or if this is significantly affected by transient noise sources related to urban activities. The analysis of the spectrograms of the recorded components (Figure 16) shows patterns that are reasonably uniform over time.
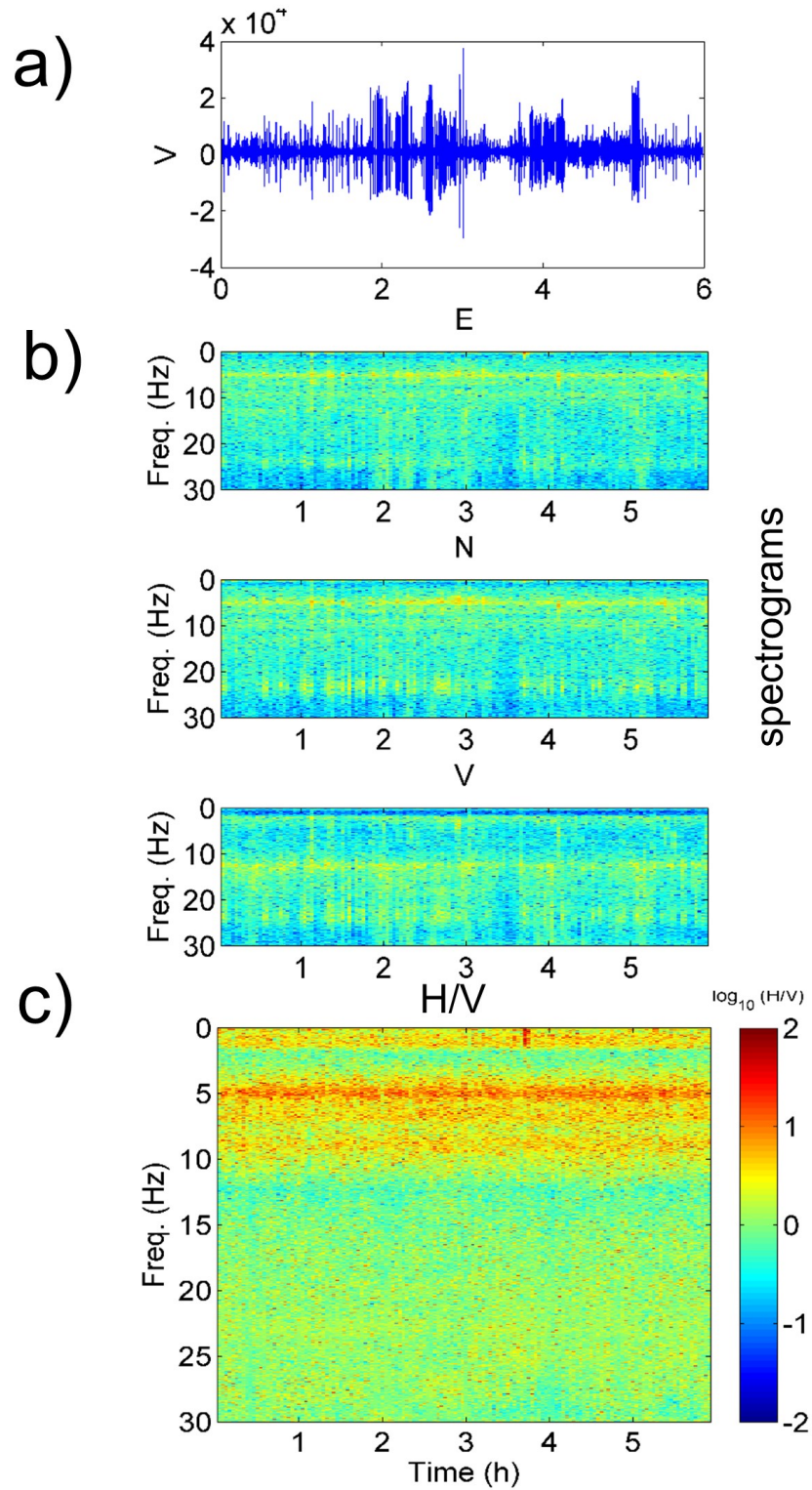
Figure 16 – Time-frequency analysis of single-station passive noise recording. a) Vertical component recording: the peaks correspond to the hammer blows of the active experiments. b) spectrograms of the east-west (E), north-south (N) and up-down (V) component recordings. c) H/V ratio over time.

As earlier anticipated, the acquired passive traces were processed with the aim of

- estimating the H/V ratio of recorded noise, thus identifying the fundamental frequency of resonance of the site (Nakamura, 1989), thanks to the application of classical H/V methods (as implemented in Geopsy software, www. geopsy.org; classical H/V of Fäh et al., 2001).

- estimating the ellipticity of Rayleigh wave as a function of frequency, by resorting to refined algorithms (Raydec, Hobiger at al., 2009; time-frequency method, Poggi and Fäh, 2009; wavelet-based time-frequency method as implemented in Geopsy software). These methods aim at eliminating the contributions of other waves besides Rayleigh waves, to obtain a more reliable estimation of Rayleigh wave ellipticity when compared to the classical H/V technique.

The obtained results are shown in Figure 17a. All applied techniques yield similar H/V or ellipticity curves, with pronounced peaks in the ranges 0.5 – 1.5 Hz (with two "summits", at 0.7 and 1.2 Hz), and 4 – 10 Hz, and deep troughs at 2 and 12 Hz. Although the portion at low frequencies (< 3 Hz) presents a good resemblance with the closest H/V measurements from the 2013 SED survey (Figure 17b, 17c), at higher frequencies dissimilarities are observed, probably witnessing lateral variations in the shallower subsurface.
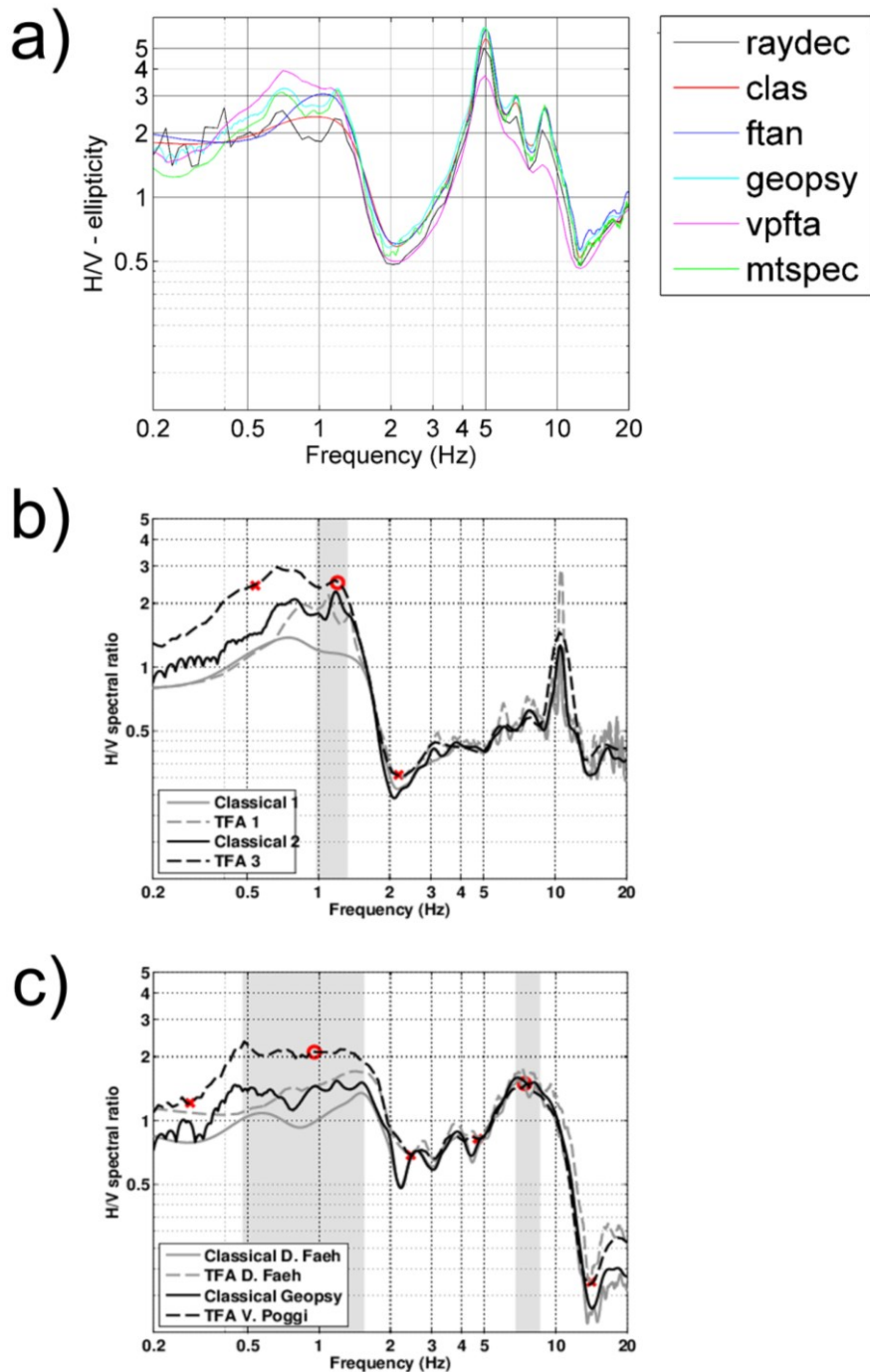
Figure 17 – a) H/V ratio and ellipticity curves obtained from the processing of noise recording data, using several algorithms. For comparison, the H/V results from the closest measurement points from the 2013 SED survey are also displayed: b) 50 m east and c) 90 m north-north-west (also shown in Figure 2).

5   Surface wave Data Inversion

The retrieved phase velocity dispersion curves of Rayleigh and Love waves, and the ellipticity characteristics of Rayleigh waves (sections 3.4, 4) were inverted for a 1D profile of the seismic

properties of the subsurface. The inversion was performed using the Dinver software of the Geopsy suite that implements an Improved Neighborhood Algorithm (Wathelet, 2008).

5.1 Inversion target

In detail, the target of the inversion consists of:
- Love wave dispersion curve, including only the fundamental mode, as obtained from the *f-k* analysis of the suitable active data (section 3.4.5)
- Rayleigh wave dispersion curve, including the modes from the fundamental to the 4th higher, as obtained from the *f-k* analysis of the suitable active data (sections 3.4.3 and 3.4.6);
- Ellipticity curve for the fundamental mode of Rayleigh waves. At high frequencies (12 – 20 Hz), the fundamental mode ellipticity curve obtained with WaveDecActive (Maranò et al., 2017, section 3.4.4) was used; at low frequencies (0.2 – 12 Hz) the ellipticity curve from passive recordings (processed with Raydec, section 4, Figure 17a) was reasonably attributed to the fundamental mode and fed to the inversion process. Data points belonging to either peaks or troughs (0.5-1.2, 1.6 - 3 Hz, 4.2 - 8 Hz, 12 - 16 Hz) were later removed to allow for the presence of singularities (Hobiger et al., 2013).

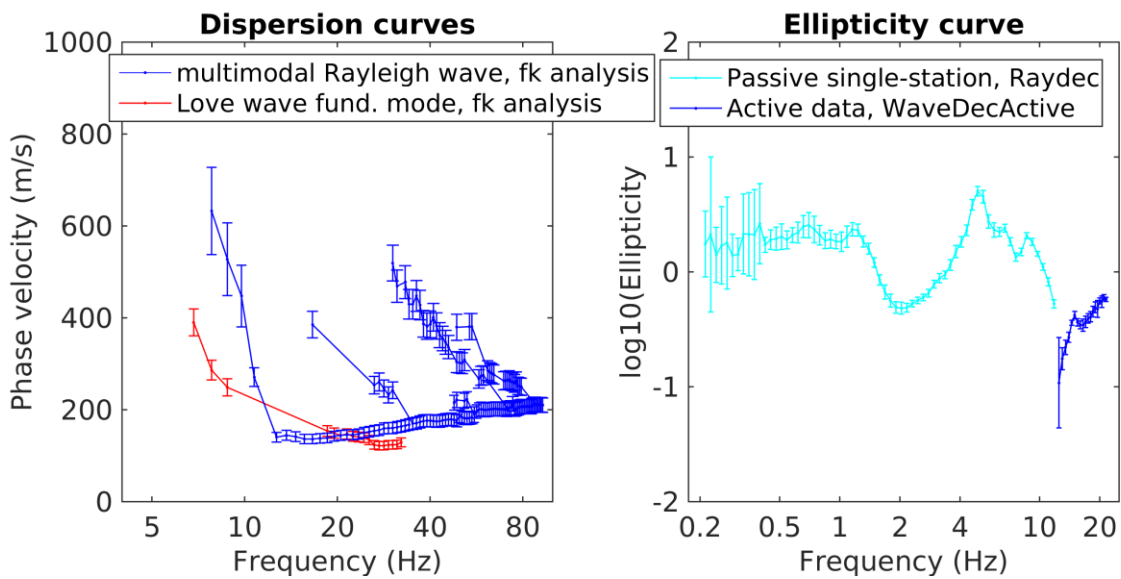Figure 18 presents all the curves considered for the final inversion process.

Figure 18 – Target of the surface wave data inversion process. Left: inverted Love wave and multimodal Rayleigh wave dispersion curves. Right: fundamental mode Rayleigh wave ellipticity

Considering the different frequency bands covered by phase velocity (7 – 90 Hz) and ellipticity data (0.2 – 20 Hz), partly overlapping, the intent is to exploit mainly the dispersion curve information for a detailed characterization of the shallow subsurface (first 30 m of depth), and to rely on the low frequency ellipticity points to estimate the depth of the interface between quaternary sediments and Molasse, and possibly the deeper boundary between the Molasse and the underlying marls of the Malm group.

Both ellipticity and dispersion curves were resampled using 150 points between 0.2 and 100 Hz, on a logarithmic scale. The ellipticity information was given lower weight (0.1) than the dispersion curves (1) in the contribution to the overall misfit value.

5.2 Parameterization of the model space

For the parameterization of the subsurface model, after a number of preliminary tests, two different strategies were followed:

- The soil column is simplified as a stack of 13 homogeneous layers with fixed thickness + halfspace The layers' fixed thicknesses increase logarithmically with depth. The soil bulk densities were fixed a priori, incrementing from 1700 kg/m^3 (near-surface) to 2700 for the deepest layer. Seismic velocities are left free to vary: V_S, V_P ranges are quite wide (generally set in a ±50% interval with respect to a central value, itself increasing with the layer's depth). For the deepest formations, modeling the Molasse and the Malm group, the velocity interval and density values were defined taking into consideration relevant lithological information (Sommaruga et al., 2012; Zappone & Bruijn, 2012). Considering the indications from the active data processing (section 3.4.3) and available geological information (Figure 22c, left), we allowed for a S-wave velocity inversion at the very near-surface; apart from this exception, for the other layers we forced a velocity increase with depth. The indication of a shallow water table (from seismic refraction interpretation, section 3.4.2) was taken into account when defining the Poisson's ratio range (extended to 0.49 for the surficial, possibly saturated layers).

- The soil column is simplied as a stack of 6 homogeneous layers with variable thickness + halfspace. Taking into account the available geological information (GeoMol project, 2016; Klingelé, 2012; Swisstopo 1:25000 geological atlases, 2017), the shallowest 4 layers were dedicated to model the complex structure of the near-surface (approx. < 30 m), including the probable S-wave velocity inversion. Below, the 5th layer models the deeper sedimentary formation reaching the Molasse, which corresponds to the 6th layer; the halfspace models the underlying Malm group. The velocity and depth ranges for these deep formations were defined taking into account available geological information; in particular, the map of sedimentary cover of E. Klingelé (2012), for the depth of the upper interface of the Molasse, the GeoMol model for its lower interface, the SAPHYR database (Zappone & Bruijn, 2012) and the Atlas of the Swiss Molasse (Sommaruga et al., 2012) for the feasible velocity ranges for the Molasse and the Malm group. The indication of a shallow water table (from seismic refraction interpretation, section 3.4.2) was taken into account when defining the Poisson's ratio ranges (extended to 0.49 for the surficial, possibly saturated layers). The soil bulk densities were fixed a priori, incrementing from 1700 kg/m^3 (near-surface) to 2700 for the deepest layer.

For both strategies, we ran an inversion process testing 400000 models in total, 300000 in the initial iteration of random search and 100000 in the final stage of refinement driven by the neighborhood algorithm. The results are shown and commented in the following section.

5.3 Inversion results

Figures 19-21 compare the results obtained following the two parameterization strategies: the one adopting variable thicknesses (Figure 19, 21 left), and that imposing fixed thicknesses (Figure 20, 21 right). The main outcome is that the former approach (variable thicknesses) allows achieving a significantly lower misfit (RMSe = 1.09, as opposed to RMSe = 1.53 of fixed thicknesses strategy). In fact, the soil column at SBIK sites is likely characterized by significant velocity contrasts (particularly at large depths, at the interfaces sediments-Molasse and Molasse-Malm group), which are appropriately modeled by a variable thickness approach; vice versa, the fixed thicknesses parameterization is more suitable for gradual velocity increments, which apparently do not fit SBIK site.

Focusing on the data fit (Figures 19, 20), both approaches allow a fairly good match of the Rayleigh and Love wave dispersion curves, which constrain the near-surface; the reconstruction of the shallow velocity models is somehow similar (Figure 21c). Both strategies consistently identify a low-velocity layer at around 1-4 m depth. However, only the variable thickness approach fits properly the ellipticity curve (Figure 19), following all its singularities thanks the reconstruction of the V_S contrasts between sediments and Molasse (around 170 m depth), and between the latter and the Malm group (approx. 700 m depth; Figure 21a,b). Vice versa, the fixed thicknesses strategy is not able to model the low-frequency singularities of the ellipticity curve (Figure 20).

The variable thicknesses parameterization was therefore preferred to produce the final inversion results: we ran for this purpose 19 additional inversion processes (besides that presented in Figure 19), with the same subsurface parameterization and inversion target (testing again 400000 models in each inversion). The minimum achieved RMSes range between 1.08 and 1.13 (median 1.10). We then selected the best velocity model from each inversion run, obtaining 20 best fitting and mutually independent velocity profiles (Figures 22, 23). These models are considered as the final inversion results and are commented in the following section
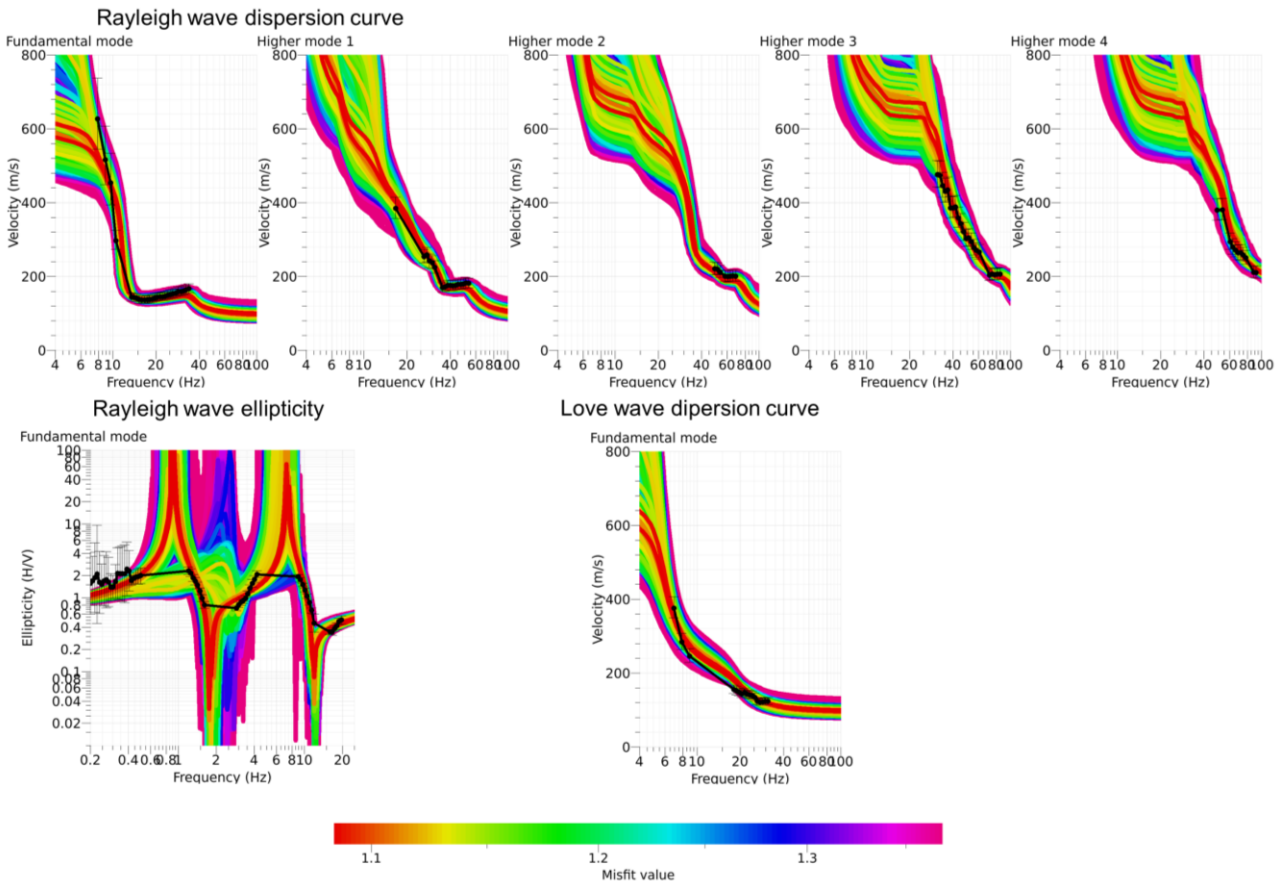
Figure 19 – Fitting of experimental data (black dots) allowed by the inversion run adopting a variable thickness parameterization. Note that the experimental curves are represented by black dots only; the black line simply connects the data points, but it is not the target of the inversion.
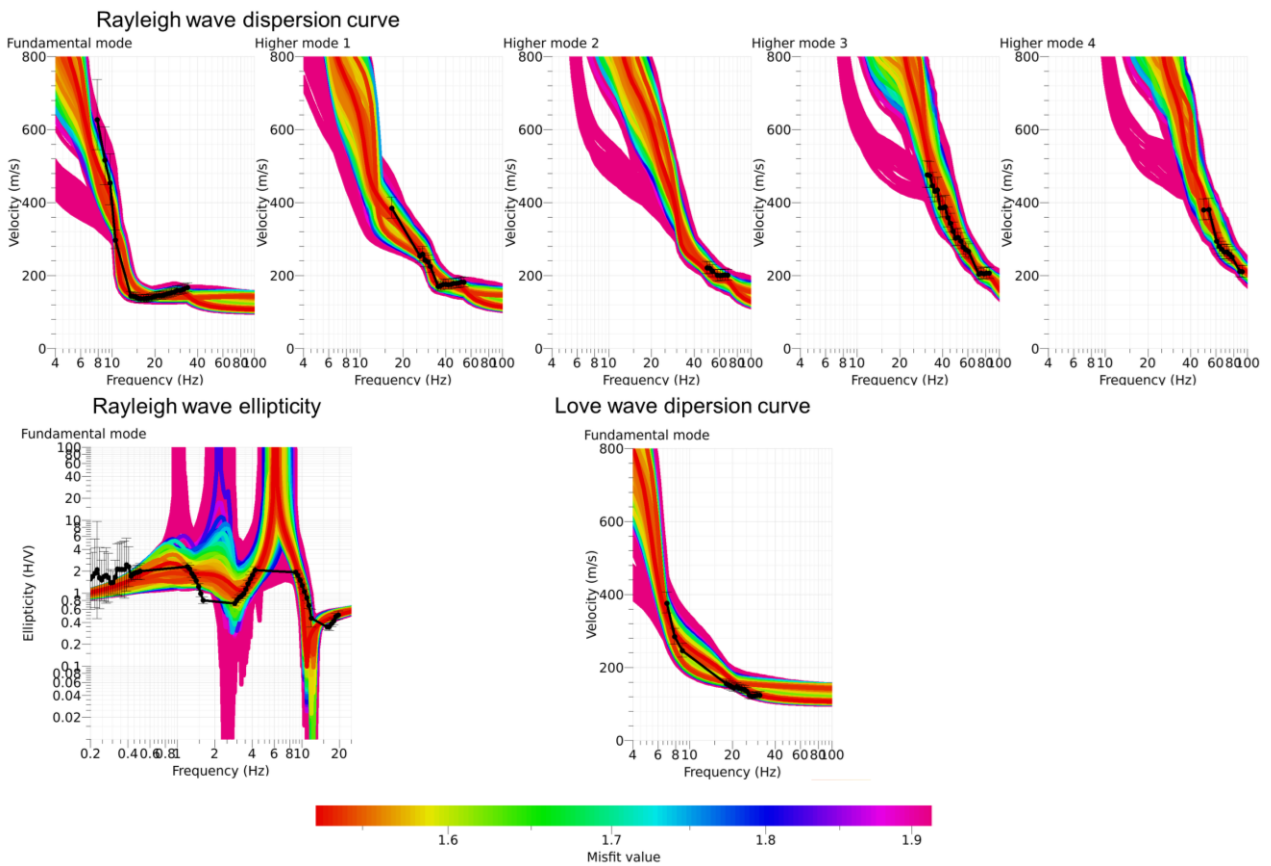
Figure 20 – Fitting of experimental data (black dots) allowed by the inversion run adopting a fixed thickness parameterization. Note that the experimental curves are represented by black dots only; the black line simply connects the data points, but it is not the target of the inversion.
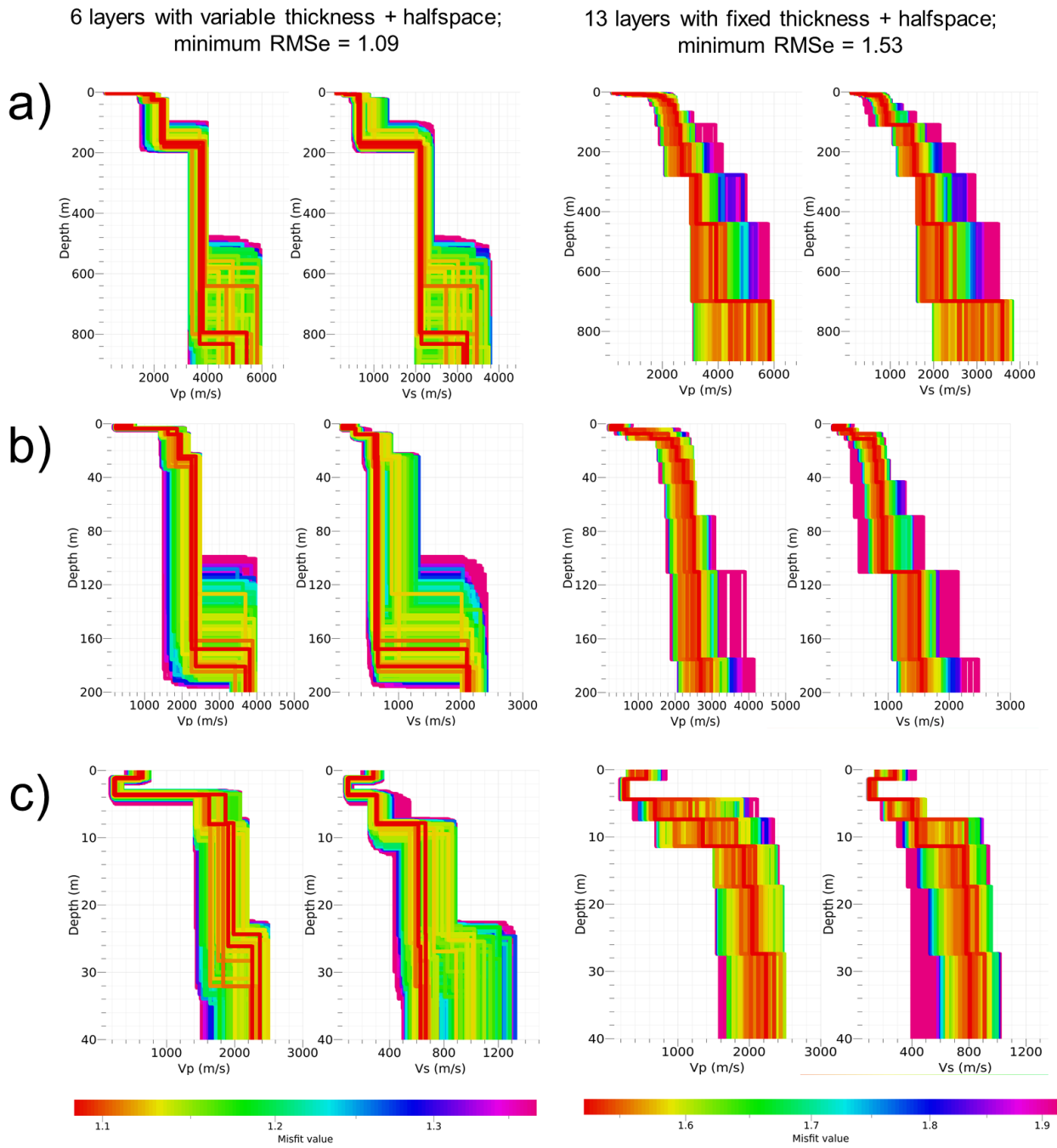
Figure 21 – Best performing models from the variable thickness (left panels) and fixed thickness (right panels) inversion runs. a) full velocity profiles; b,c) zoom of the intermediate and shallow depth ranges. The color scale is the same of Figure 19 and 20, respectively

30

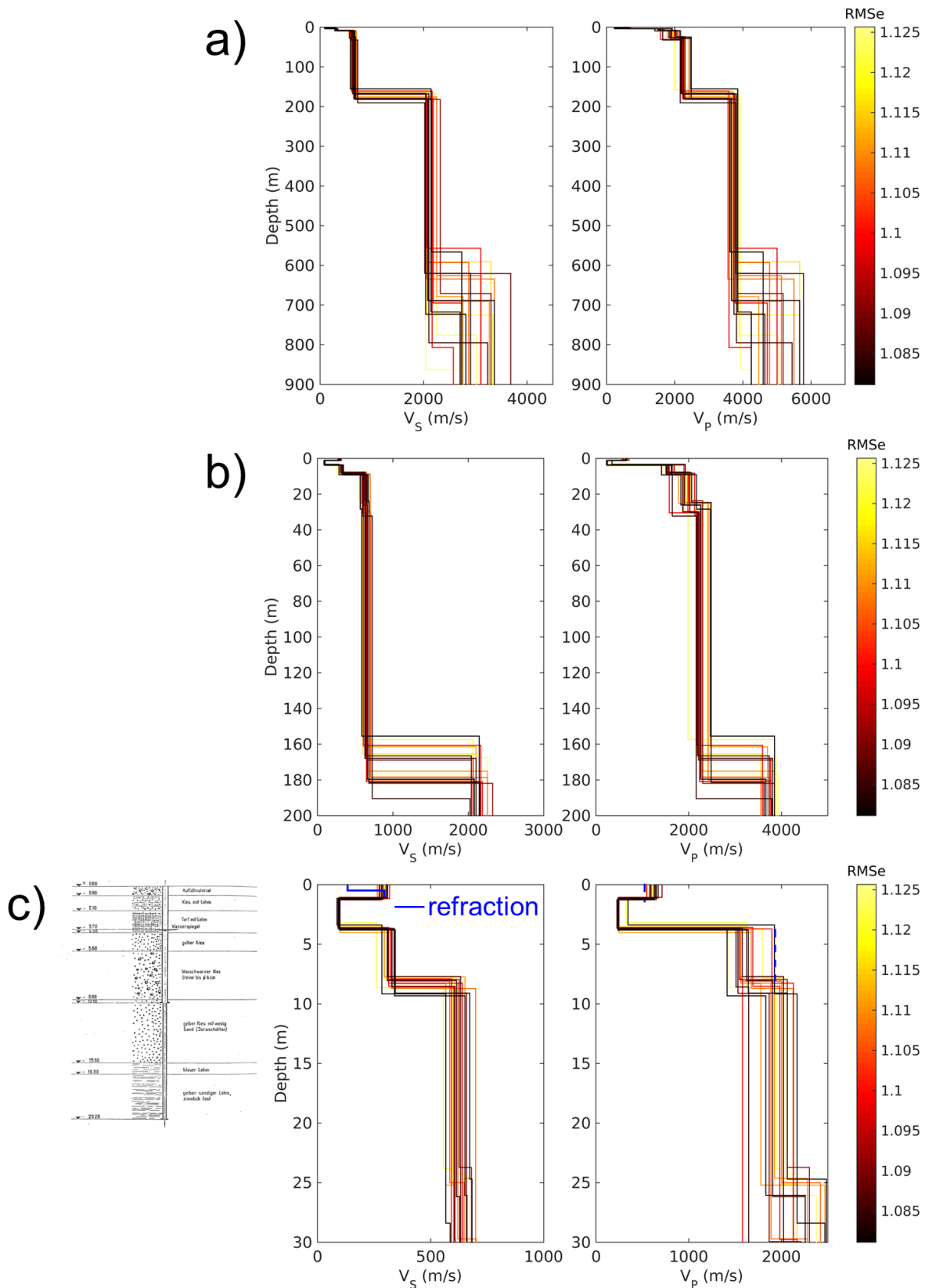*Figure 22 – 20 best fitting velocity models, each obtained from a different inversion run adopting the variable thickness parameterization. For each inversion run, 400000 models were tested. b,c) zoom of the intermediate and shallow depth ranges. In (c) we include also the stratigraphic log from a shallow borehole drilled 25 m east of the active array centre (from Geoportal Kanton Bern, 2016)*
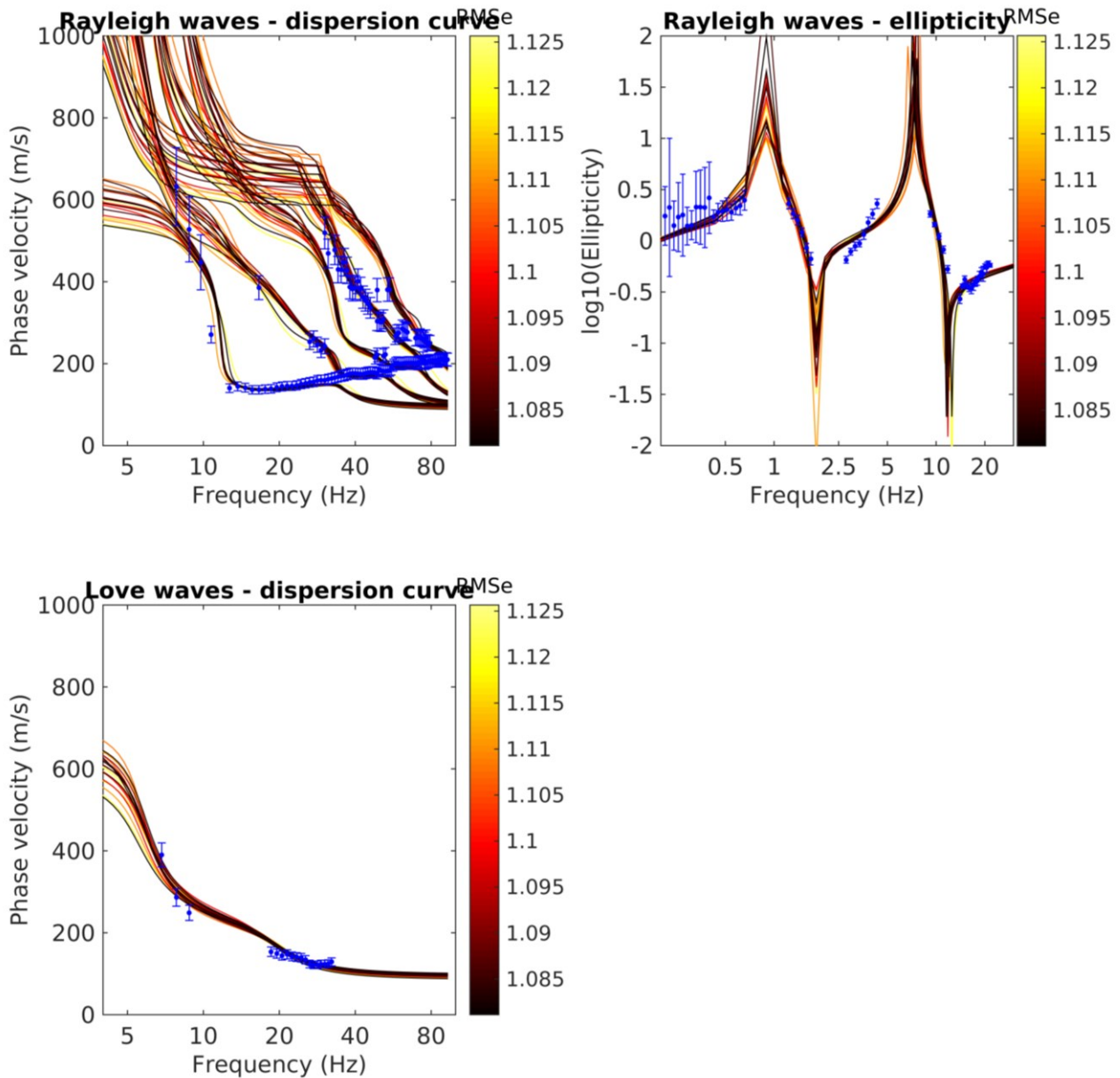
Figure 23 – Comparison between the synthetic curves from the best 20 velocity models (black-to-yellow lines) and the experimental curves (blue data points). Note that the latter are represented in their original frequency vector (before the homogeneous resampling in logarithmic scale).

6   Interpretation of the velocity profiles

6.1 Velocity profiles

The best performing velocity models of Figure 22, each obtained from a different inversion run, show globally a consistent trend. In the near-surface (Figure 22c), the shallow layer (1 m thick, $V_S = 295$ m/s, $V_P = 630$ m/s) is to be identified as the soil cover of the green area where the survey was carried out (Figure 3). We should note that these velocities are similar to those obtained from the P- and S-wave refraction data interpretations (blue lines in Figure 21c); as for S-wave refraction, this identifies

a topmost layer with V_S = 133 m/s and 0.5 m deep; the surface wave survey, with an inter-geophone distance of 1.7 m, cannot resolve this very shallow layer.

Below, we find a velocity inversion, with a slower layer having V_S = 95 m/s and extending down to circa 3.8 m depth. This soft layer is to be associated with the loam and turf formations appearing in the same depth range in the logs of nearby boreholes (the one displayed in Figure 22c was drilled 25 m east of the centre of the geophone array; Geoportal Kanton Bern, 2016). Further below, V_S increases again to 325 m/s in the depth interval 3.8-8.5 m, a layer described as composed by gravel in the geotechnical log. The values of V_P range between 1550 and 1950 m/s (here again with some agreement with the result of P-wave refraction), compatible with those of a saturated granular formation; the depth of the water table is therefore around 3.8 m, in agreement with the indication from the borehole.

At ~8.5 m depth a sharp velocity increase is met (from 325 to 550-700 m/s of V_S); this increment is probably to be associated to the interface between the surficial layers and the more compact alluvial deposit of the Juraschotter (according to the borehole log). The S-wave velocity remains comprised between 585 and 725 m/s down a depth of 155-185 m (mean value 172 m), the identified interface between the upper alluvial sediments and the underlying Molasse (V_S = 2050-2250 m/s). These depth values are at the upper end of the range (80-160 m) indicated by the sediment-to-bedrock interface reconstruction by Klingelé (2012; see Figure 2), obtained for the whole Swiss Molasse basin combining gravimetric data with deep borehole logs. The 6th layer, modeling the Molasse, extends down to a depth of 600-800 m (mean value 682 m); this interval is in agreement with the GeoMol model (GeoMol project, 2016), showing a maximum depth for the Molasse below Biel of around 700 m.

It should be noted that, while the reconstruction of the shallow subsurface is quite well constrained and consistent among the selected best models, its uncertainty becomes significant at large depths (see Figure 22, 21a), where the inversion is driven only by ellipticity data and lacks information about the deep formations' velocities from dispersion curves.

6.2 Quarter-wavelength representation

The quarter-wavelength velocity representation (V_S^{QWL}; Joyner et al., 1981) attributes to each frequency the average velocity at a depth equal to ¼ of the corresponding wavelength. V_S^{QWL} can be used as direct proxy for the local site characterization, as it physically relates the resolution on ground parameters with the characteristics of the propagating wave-field at the discrete frequencies. The derived quarter-wavelength impedance contrast (IC^{QWL}; Poggi et al., 2012) is the ratio between two quarter-wavelength average velocities, from the top and bottom part of the velocity profile respectively, at a given frequency; it is a powerful tool to assess the influence of resonance phenomena in soft sediment sites.

Figure 24 shows the average (over the population of the selected 20 best subsurface models) quarter-wavelength velocity (centre) and impedance contrast (bottom) representations. The obtained Vs30 (which is the average velocity corresponding to a quarter-wavelength of 30 m) is 374 m/s.

The IC^{QWL} graph shows two peaks at 0.8 and 5-9 Hz, to be associated with the impedance contrasts in the deep (sediments-Molasse and Molasse-Malm group interfaces) and shallow (at 3.8, 8.5 m depth) subsurface, respectively.
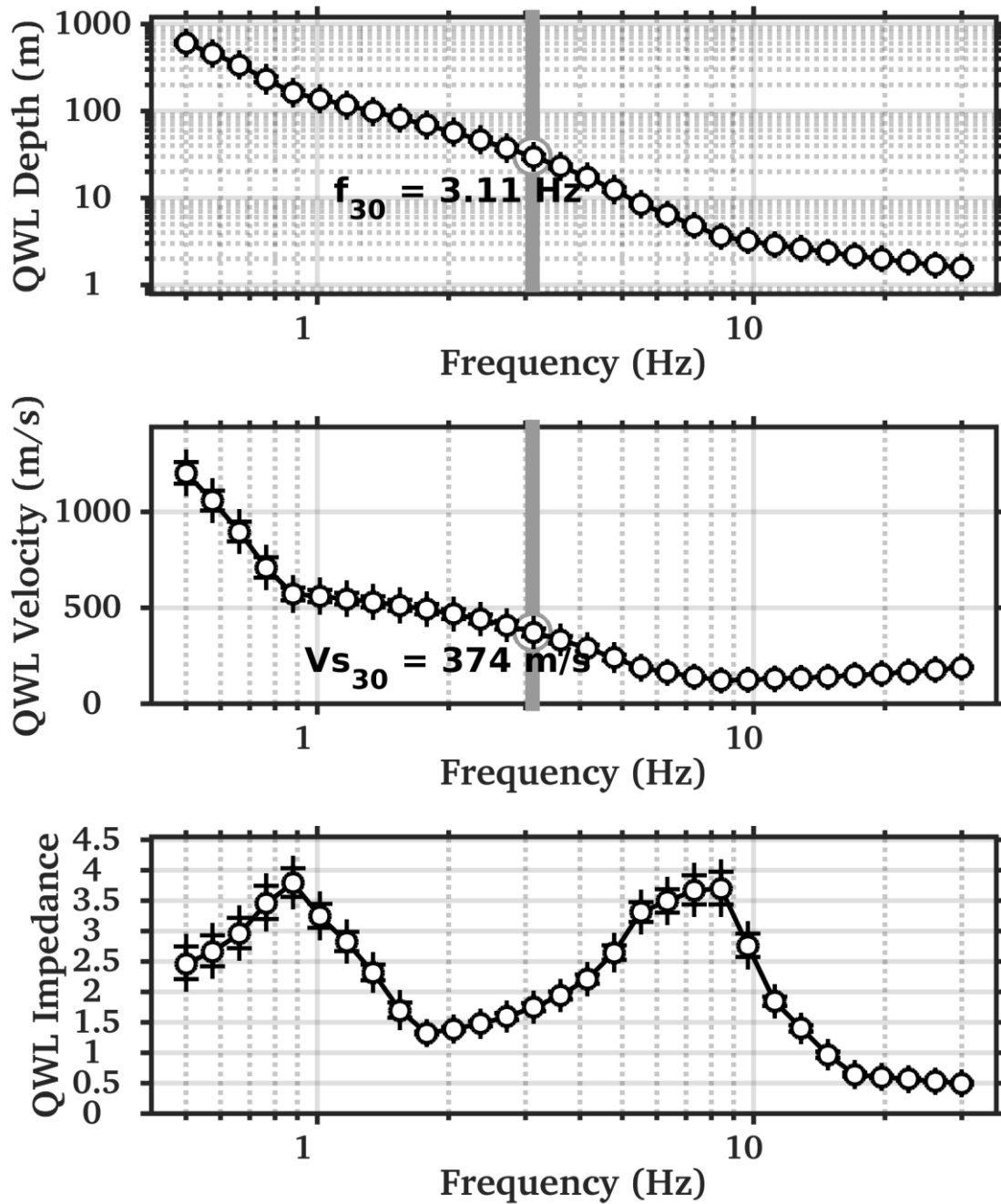
Figure 24 – Average quarter-wavelength representation of the selected velocity profiles (Figure 21). Top: depth; center: velocity; bottom: impedance contrast. The gray line in the top and center panel refers to Vs₃₀.

6.3 SH transfer function.

The theoretical SH-wave transfer function for vertical propagation (Roesset, 1970) was computed for the selected models, (Figure 21). The transfer functions were also corrected for the Swiss reference rock model (Poggi et al., 2011), following Edwards et al. (2013).

These are compared (Figure 25) with the empirical amplification function obtained from spectral modeling (ESM; Edwards et al., 2013; Michel et al., 2014), relying on 25 events in the 2 – 8 Hz frequency band, decreasing to 4 events at lower and higher frequencies (as of 16.04.2018). The agreement between simulated and empirical amplification functions is relatively good. At low frequencies (< 3 Hz), the simulated curves somehow reproduce the (broad) peaks of the empirical amplification functions at 0.8 and 1.25 Hz, related to the impedance contrasts Molasse-Malm group, and sediments-Molasse, respectively. The peak at ~2.5 Hz in the synthetic curves is composed by the 1st higher order peaks of the two resonance frequencies mentioned above, and has some agreement with a similar feature in the empirical amplification function. The main feature of the empirical curve is a tall (reaching amplification factors > 10) and broad peak between 4-8 Hz, which corresponds to the shallow velocity contrasts at approx. 3.8 and 8.5 m depth (interfaces between turf and underlying gravel, and between the shallow formations and the more compact Juraschotter, respectively). Here again, the simulated curves manage to replicate this feature, reaching similar amplification values at its top. The further peak at ~19 Hz appears to be a higher order peak of the latter, and it is matched by an analogous feature in the synthetic curves, although centered at slightly higher frequencies (around 22.5 Hz)
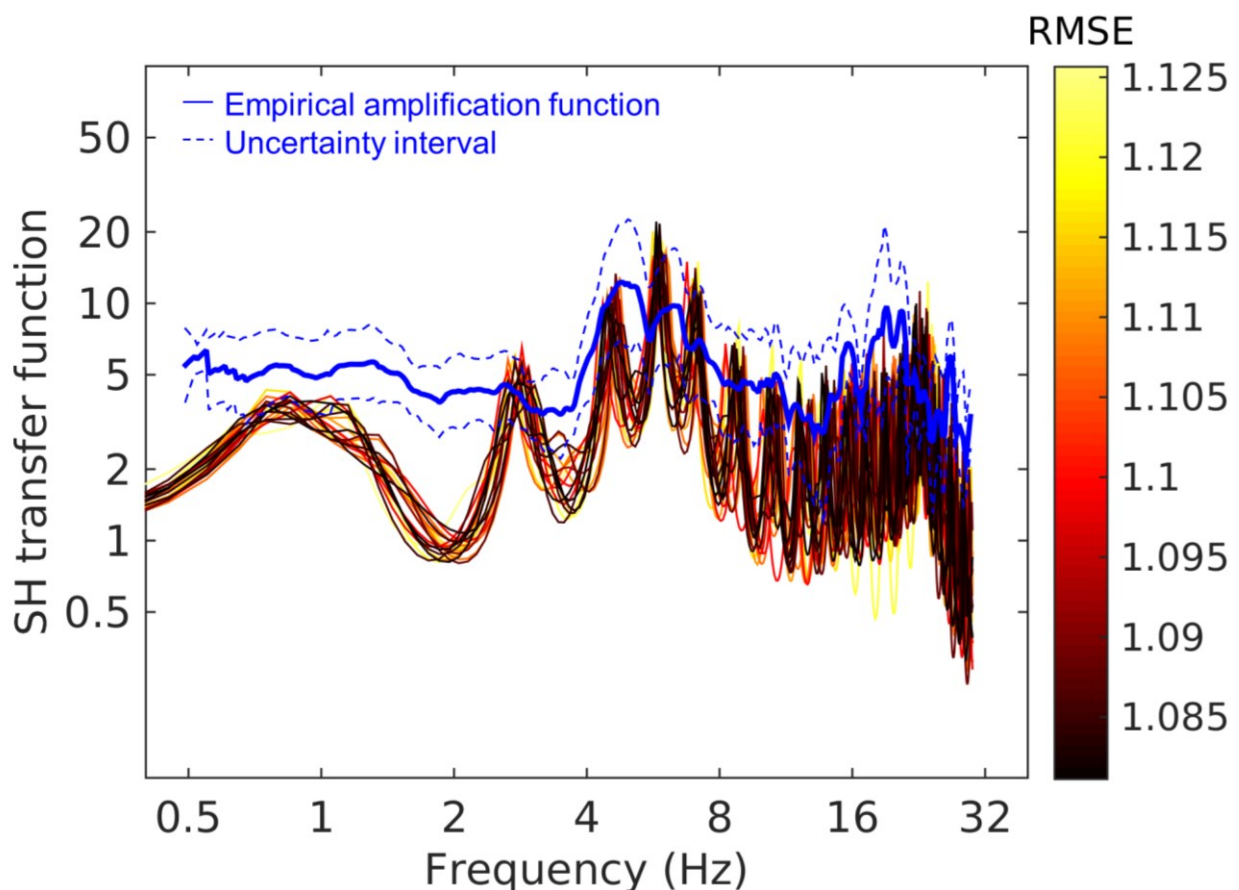

Figure 25 – Modeled SH transfer functions (colored lines) from the selected velocity profiles, corrected for the Swiss reference rock model, compared with the empirical amplification function for SBIK (blue line).

7   Conclusions

Active seismic measurements and a single-station noise recording were performed to characterize the structure of the subsurface below the SSMNet station SBIK (Biel, BE). Active data were processed to derive Rayleigh and Love wave dispersion curves, Rayleigh wave ellipticity curve, and to identify the direct and refracted first break arrivals of P- and SH- waves. Passive data were analyzed to estimate the ellipticity curve of Rayleigh waves.

The velocity profile derived from the inversion process includes a surficial layer with $V_S = 280$ m/s and 1 m thick (soil cover); below, a softer layer ($V_S = 95$ m/s) composed of turf and loam, is met (depth 1 – 3.8 m). Further below, as turf and loam are replaced by gravels, the Shear-wave velocity sharply increases assuming a value of 325 m/s in the depth interval 3.8 – 8.5 m. The upper interface of this layer coincides with the water table. The S-wave velocity increases then to 550-725 m/s in a depth range extending down to 155-180 m depth (thick aggradation sediments overlying the Molasse). The Molasse formation (V_S=2050-2250 m/s) should then extend from 155-180 m to 620-800 m, where the upper interface of the Malm group was located (the latter having a S-wave velocity of circa 2700-3700 m/s).

The sharp velocity contrasts at shallow depths (3.8 an 8.5 m) are responsible for a high peak at 4-8 Hz, which is found both in H/V curves and in the empirical amplification function for SBIK (where the peak reaches amplification factors > 10). The deeper interfaces sediments-Molasse and Molasse-Malm group are responsible for the peaks at 0.7 and 1.2 Hz in both the H/V graphs and in the empirical amplification function.

The obtained V_{S30} is 374 m/s, thus classifying the soil as B type according to Eurocode 8 (CEN, 2004), and as C type following SIA261 (SIA, 2014).

References

Abdel Moati W.H., D. Boiero, and L.V. Socco, 2013. A tool for fast underground characterization for trenchless pipeline construction by horizontal directional drilling technology. 11th Offshore Mediterranean Conference and Exhibition, Ravenna, Italy, March 20-22 2013.

Boiero, D., and L. V. Socco, 2010, Retrieving lateral variations from surface wave dispersion curves analysis: Geophysical Prospecting, **58**, 977–996

CEN, 2004. Eurocode 8: Design of structures for earthquake resistance – Part 1: general rules, seismic actions and rules for buildings. European Committee for Standardization, en 1998-1 edition.

Edwards, B., Michel, C., Poggi, V., and Fäh, D. , 2013. Determination of Site Amplification from Regional Seismicity : Application to the Swiss National Seismic Networks. Seismological Research Letters, 84(4).

Fäh, D., F. Kind, and D. Giardini, 2001. A theoretical investigation of average H/V ratios. GJI, 145, no. 2, 535-549.

Foti, S., Lancellotta, R., Sambuelli, L. & Socco, L.V., 2000. 'Notes on fk analysis of surface waves', *Annali di Geofisica,* **43**(6), 1199–1210.

Foti, S., Lai C.G., Rix G.J., and C. Strobbia, 2015, Surface Wave Methods for Near-Surface Site Characterization: CRC Press, Taylor & Francis Group LLC

GeoMol project, 2016. www.geomol.ch/en/geomol.html, accessed 16.11.2016.

Geoportal Kanton Bern, 2016. http://www.map.apps.be.ch/pub/synserver?project=a42pub_geolog&userprofile=geo&language=de Accessed 16.11.2016.

Hobiger, M., C. Cornou, M. Wathelet, G. Di Giulio, B. Knapmeyer-Endrun, F. Renalier, P.Y. Bard, A. Savvaidis, S. Hailemikael, N. Le Bihan, M. Ohrnberger, and N. Theodoulidis, 2013. Ground structure imaging by inversion of Rayleigh wave ellipticity: sensitivity analysis and application to European strong motion sites. GJI, 192, 207-229.

Hobiger, M., P.-Y. Bard, C. Cornou, and N. Le Bihan, 2009. Single station determination of Rayleigh wave ellipticity by using the random decrement technique (Raydec). GRL, 36, L14303

Ivanov, J., R.D. Miller, J.B. Dunbar, and J. Stefanov, 2004. Interrogating levees using seismic methods in southern Texas. SEG Int'l Exposition and 74th Annual Meeting, Denver, 10-15 October 2004, Expanded. Abstracts, 23, 1413-1416.

Joyner, W. B., Warrick, R. E., and Fumal, T. E. (1981). The effect of Quaternary alluvium on strong ground motion in the Coyote Lake, California, earthquake of 1979. Bulletin of the Seismological Society of America, 71(4):1333–1349.

Klingelé E., 2012. Systematic analysis of gravity anomalies in Switzerland. Swiss Geophysical Commission (Ed.). – Annual Report.

Marano' S., 2016. http://mercalli.ethz.ch/~marra/WaveDec/userguide_WaveDec.html

Marano', S., Hobiger M., P. Bergamo and D. Faeh, 2017. Analysis of Rayleigh Waves with Circular Wavefront: a Maximum Likelihood Approach. GJI, 210, 1570-1580.

Maraschini M., and S. Foti, 2010. A Monte Carlo multimodal inversion of surface waves. GJI, 182 (3). 1557 – 1566.

Michel, C., B. Edwards, V. Poggi., J. Burjanek, D. Roten, C. Cauzzi, and D. Faeh, 2014. Assessment of Site Effects in Alpine Regions through Systematic Site Characterization of Seismic Stations. BSSA, 104, no. 6, 2809-2826

Nakamura, Y., 1989. A Method for Dynamic Characteristics Estimation of Subsurface Using Microtremor on the Ground Surface. Quarterly Report of RTRI, vol. 30, no. 1, 25- 33.
Neducza, B., 2007, Stacking of surface waves: Geophysics, 72, 51–58.

O'Neill, A., 2003, Full-waveform reflectivity for modelling, inversion and appraisal of seismic surface wave dispersion in shallow site investigations: PhD thesis, University of Western Australia, Perth, Australia.

Park, C. B., R. D. Miller, and J. Xia, 1999. Multichannel analysis of surface waves: Geophysics, **64**, 800–808.

Poggi, V., Edwards, B., and Fäh, D. (2012). Characterizing the Vertical-to-Horizontal Ratio of Ground Motion at Soft-Sediment Sites. Bulletin of the Seismological Society of America, 102(6):2741–2756.30
Poggi, V., and D. Fäh, 2009. Estimating Rayleigh wave particle motion from three component array analysis of ambient vibrations. GJI, 180, no. 1, 251-267.

Redpath, B. B., 1973, Seismic refraction exploration for engineering site investigations: National Technical Information Service, Technical Report E-73-4.

Reynolds, J.M., 2011, An introduction to applied and Environmental Geophysics: John Wiley & Sons, Ltd.

Roesset, J. (1970). Fundamentals of soil amplification. In Hansen, R. J., editor, Seismic Design for Nuclear Power Plants, pages 183–244. M.I.T. Press, Cambridge, Mass.

SIA, 2014. SIA 261 Einwirkungen auf Tragwerke. Société Suisse des ingénieurs at des architectes, Zurich, Switzerland.

Schmelzbach C., D. Sollberger, S. A. Greenhalgh, H. Horstmeyer, H. Maurer and J.O.A. Robertsson, 2016. 9C seismic data acquisition for near-surface applications: recording, wavefrom reciprocity and 4C rotation. 78th EAGE conference and exhibition. Extended abstract WS04 B03

Socco, L.V., D. Boiero, S. Foti, and R. Wisen, 2009, Laterally constrained inversion of ground roll from seismic reflection records: Geophysics, **74**, no. 6, G35-G45.

Socco, L.V., and C. Strobbia, 2004, Surface-wave method for near-surface characterization: a tutorial: Near Surface Geophysics, **2**, no. 4, 165-185.

Sommaruga, A., Eichenberger, U. & Marillier, F. (2012): Seismic Atlas of the Swiss Molasse Basin. Edited by the Swiss Geophysical Commission. - Matér. Géol. Suisse, Géophys. 44

Sollberger D., C. Schmelzbach, C. Van Renterghem, J. O. Robertsson and S. A- Greenhalgh, 2016. Single-component elastic wavefield separation at the free surface using source- and receiver-side gradients. SEG International Exposition and 86th annual meeting, 2268 – 2273.

Swisstopo, 2017. Atlas géologique de la Suisse, 1:25000, Feuille 109.

Tokimatsu, K., 1997. Geotechnical site characterization using surface waves, in *Proceedings of the First International Conference on Earthquake Geotechnical Engineering,* pp. 1333–1368, IS-Tokyo′95, Tokyo, Balkema, Rotterdam.

Wathelet, M., 2008. An improved neighborhood algorithm: Parameter conditions and dynamic scaling. GRL, 35, no.9, 1-5.
Whiteley, R. J. and S. A. Greenhalgh, 1979. Velocity inversion and the shallow seismic refraction method. Geoexploration 17 (2). 125-141.

Zappone, A., and R. H. C. Bruijn, 2012. The Swiss atlas of physical properties of rocks (SAPHYR). Rapport Annuel 2012, Commission Suisse de Géophysique CSGP.